

**Satellite detection of severe convective storms by their retrieved vertical profiles of cloud
particle effective radius and thermodynamic phase**

Daniel Rosenfeld¹, William L. Woodley², Amit Lerner¹, Guy Kelman¹

Daniel T. Lindsey³

¹Institute of Earth Sciences, The Hebrew University of Jerusalem, Israel

²Woodley Weather Consultants, 11 White Fir Court, Littleton CO 80127, USA

³NOAA/NESDIS/RAMMB, Fort Collins, CO

Second revision

Submitted to JGR in August 2007

1 ABSTRACT

2

3 A new conceptual model that facilitates the inference of the vigor of severe convective
4 storms, producing tornadoes and large hail, by using satellite-retrieved vertical profiles of cloud
5 top temperature (T) – particle effective radius (r_e) relations is presented and tested. The driving
6 force of these severe weather phenomena is the high updraft speed, which can sustain the
7 growth of large hailstones and provide the upward motion that is necessary to evacuate the
8 violently converging air of a tornado. Stronger updrafts are revealed by the delayed growth of r_e
9 to greater heights and lower T , because there is less time for the cloud and rain drops to grow
10 by coalescence. The strong updrafts also delay the development of a mixed phase cloud and its
11 eventual glaciation to colder temperatures. Analysis of case studies making use of these and
12 related criteria show that they can be used to identify clouds that possess a significant risk of
13 large hail and tornadoes. Although the strength and direction of the wind shear are major
14 modulating factors, it appears that they are manifested in the updraft intensity and cloud shapes,
15 and hence in the T - r_e profiles. It is observed that the severe storm T - r_e signature is an extensive
16 property of the clouds that develop ahead in space and time of the actual hail or tornadic storm,
17 suggesting that the probabilities of large hail and tornadoes can be obtained at substantial lead
18 times. Analyses of geostationary time series indicates lead times of up to 2 hours.

19 **1. Introduction**

20

21 This study presents a new conceptual model that facilitates the detection of the vigor of
22 convective storms by remote sensing from satellites, based on the retrieved vertical profiles of
23 cloud-particle effective radius and thermodynamic phase. Severe convective storms are defined
24 by the US National Weather Service as having wind gusts > 58 mph, hail > 3/4 inch in
25 diameter, or producing tornadoes. A major driving force of all these severe weather phenomena
26 is the high updraft speeds, which can sustain the growth of large hailstones, provide the upward
27 motion that is necessary for evacuating vertically the violently converging air of a tornado, or
28 complemented strong downward motion, which results in downbursts and intense gust fronts.

29 Wind shear provides additional energy for spinning up tornadoes and for sustaining the
30 dynamics of super-cell storms and squall lines that can re-circulate large hailstones and produce
31 damaging winds. The respective roles of convective potential available energy (CAPE) and the
32 0-6 km vertical wind shear have been the main predictors for severe convective storms
33 (Rasmussen and Blanchard, 1998; Hamill and Church, 2000; Brooks et al., 2003). The wind
34 shear and low-level storm relative helicity (rotation of the wind vector) are of particular
35 importance for inducing strong (At least F2) tornadoes (Dupilka and Reuter, 2006a and 2006b).
36 However, even with small helicity, a steep low level lapse rate and large CAPE can induce
37 strong tornadoes due to the large acceleration of the updrafts already at low levels (Davis,
38 2006). This underlines the importance of the updraft velocities in generating the severe
39 convective storms, and the challenges involved in their forecasting based on sounding data
40 alone.

41 The conceptual model of a satellite-observed severe storm microphysical signature,
42 which is introduced in this paper, is based on the satellite-retrieved microphysical signature of
43 the updraft velocity on the developing convective elements that have the potential to become
44 severe convective storms, or already constitute the feeders of such storms. The severe storm
45 microphysical signature, as manifested by the vertical profile of cloud-particle effective radius,
46 is caused by the greater updrafts delaying to greater heights the conversion of cloud drops to
47 hydrometeors and the glaciation of the cloud. The greater wind shear tilts the convective towers
48 and often deflects the strongly diverging cloud tops from obscuring the feeders. This allows the
49 satellite a better view of the microphysical response of the clouds to the strong updrafts. This
50 satellite severe storm signature appears to primarily reflect the updraft speed of the growing
51 clouds, which is normally associated with the CAPE. But wind shear is as important as CAPE
52 for the occurrence of severe convective storms, in addition to helicity that is an important

53 ingredient in intense tornadoes. It is suggested that the effectiveness of the satellite retrieved
54 severe storm signature and inferred updraft speed may not only depend on the magnitude of the
55 CAPE, but also on the wind shear, and perhaps also on the helicity. This can occur when some
56 of the horizontal momentum is converted to vertical momentum in a highly sheared
57 environment when strong inflows are diverted upward, as often happens in such storms. While
58 this study focuses on exploring a new concept of satellite application, eventually a combined
59 satellite with sounding algorithm is expected to provide the best skill.

60

61 Section 1.1 of this paper provides a short review of the relation between the updraft
62 velocity and the vertical evolution of mixed phase precipitation and the glaciation of convective
63 clouds. Section 2.1 introduces the conceptual model for the methodology for the satellite
64 retrieval of a severe storm microphysical signature and supports it on the basis of previous
65 observations and theoretical considerations. Section 2.2 reviews the satellite methodology to
66 retrieve the vertical evolution of cloud properties and precipitation forming processes. Sections
67 2.3 and 2.4 apply this methodology qualitatively to microphysically continental and maritime
68 convective clouds. Section 2.5 considers the role of the vertical wind shear. A quantitative
69 application is tested in Section 3 on a data set of satellite measurements and severe storm
70 reports. The results and their significance are discussed in Section 4.

71

72 **1.1 Direct observations of cloud top dynamics for inferences of updraft velocities and** 73 **storm severity**

74 Updraft speeds are the most direct measure of the vigor of a convective storm. The
75 updraft speeds of growing convective clouds can be seen in the rise rate of the cloud tops, or
76 measured from satellites as the cooling rate of the tops of these clouds. A typical peak value of
77 updrafts of severe storms exceeds 30 ms^{-1} (e.g., Davies-Jones, 1974). Such strong updrafts are
78 too fast to be detected by a sequence of geostationary satellite images, because even during a 5
79 minute rapid scan an air parcel moving at 30 ms^{-1} covers 9 km if continued throughout that time
80 (super-rapid scans of up to one per 30 – 60 s can be done, but only for a small area and not on a
81 routine operational basis). But such strong updrafts occur mainly at the supercooled levels,
82 where the added height of 9 km will bring the cloud top to the tropopause in less than 5
83 minutes. In addition, the cloud segments in which such strong updrafts occur are typically
84 smaller than the resolution of thermal channels of present day geostationary satellites (5 to 8
85 km at mid latitudes). This demonstrates that both the spatial and temporal resolutions of the
86 current geostationary satellites are too coarse to provide direct measurements of the updraft

87 velocities in severe convective clouds. The overshooting depth of cloud tops above the
88 tropopause can serve as a good measure of the vigor of the storms, but unfortunately the
89 brightness temperatures of overshooting cloud tops does not reflect their heights due to the
90 generally isothermal nature of the penetrated lower stratosphere.

91 Overshooting severe convective storms often develop a V shape feature downwind of
92 their tallest point, which appears as a diverging plume above the anvil top (Heymsfield et al.,
93 1983; McAnn, 1983). The plume typically is highly reflective at 3.7 μm , which means that it is
94 composed of very small ice particles (Levizzani and Setvák, 1996, Setvák et al., 2003). A warm
95 spot at the peak of the V is also a common feature, which is likely caused by the descending
96 stratospheric air downwind of the overshooting cloud top. Therefore, the V-shape feature is a
97 dynamic manifestation of overshooting tops into the lower stratosphere when strong storm-
98 relative winds occur there. The observation of a V-shape feature reveals the existence of the
99 combination of intense updrafts and wind shear. Adler et al. (1983) showed that most of the
100 storms that they examined in the US Midwest (75%) with the V-shape have severe weather, but
101 many severe storms (45%) do not have this feature. Adler et al. (1983) showed also that the rate
102 of expansion of storm anvils was statistically related positively to the occurrences of hail and
103 tornadoes. All this suggests that satellite inferred updraft velocities and wind shear are good
104 indicators for severe storms. While wind shear is generally easily inferred from synoptic
105 weather analyses and predictions, the challenge is the inference of the updraft intensities from
106 the satellite data. The manifestation of updraft velocities in the cloud microstructure and
107 thermodynamic phase, which can be detected by satellites, is the subject of the next section.
108

109 **1.2 Anvil tops with small particles at -40°C reflecting homogeneously-glaciating clouds**

110

111 Small ice particles in anvils or cirrus clouds typically form as a result of either vapor
112 deposition on ice nuclei, or by homogeneous ice nucleation of cloud drops which occurs at
113 temperatures colder than -38°C. In deep convective clouds heterogeneous ice nucleation
114 typically glaciates the cloud water before reaching the -38°C threshold. Clouds that glaciate
115 mostly by heterogeneous nucleation (e.g. by ice multiplication, ice-water collisions, ice nuclei
116 and vapor deposition) are defined here as glaciating heterogeneously. Clouds in which most of
117 their water freezes by homogeneous nucleation are defined here as undergoing homogeneous
118 glaciation. Only a small fraction of the cloud drops freezes by interaction with ice nuclei,
119 because the concentrations of ice nuclei are almost always smaller by more than four orders of
120 magnitude than the drop concentrations (ice nuclei of $\sim 0.01 \text{ cm}^{-3}$ whereas drop concentrations

121 are typically $> 100 \text{ cm}^{-3}$) before depletion by evaporation, precipitation or glaciation. Therefore,
122 most drops in a heterogeneously glaciating cloud accrete on pre-existing ice particles, or
123 evaporate for later deposition on the existing cloud ice particles. This mechanism produces a
124 glaciated cloud with ice particles that are much fewer and larger than the drops that produced
125 them. In fact, heterogeneous glaciation of convective clouds is a major precipitation-forming
126 mechanism.

127 Heterogeneously glaciating clouds with intense updrafts ($> 15 \text{ ms}^{-1}$) may produce large
128 supersaturations that, in the case of a renewed supply of CCN from the ambient air aloft, can
129 nucleate new cloud drops not far below the -38°C isotherm, which then freeze homogeneously
130 at that level (Fridlind et al., 2004; Heymsfield et al., 2005). In such cases the cloud liquid water
131 content (LWC) is very small, not exceeding about 0.2 g m^{-3} . This mechanism of homogeneous
132 ice nucleation occurs, of course, also at temperatures below -38°C , and is a major process
133 responsible for the formation of small ice particles in high-level strong updrafts of deep
134 convective clouds, which are typical of the tropics (Jensen and Ackerman, 2006).

135 Only when much of the condensed cloud water reaches the -38°C isotherm before
136 being consumed by other processes, can the cloud be defined as undergoing homogeneous
137 glaciation. The first in situ aircraft observations of such clouds were made recently, where
138 cloud filaments with LWC reaching half (Rosenfeld and Woodley, 2000) to full (Rosenfeld et
139 al., 2006b) adiabatic values were measured in west Texas and in the lee of the Andes in
140 Argentina, respectively. This required updraft velocities exceeding 40 ms^{-1} in the case of the
141 clouds in Argentina, which produced large hail. The aircraft measurements of the cloud particle
142 size in these two studies revealed similar cloud particle sizes just below and above the level
143 where homogeneous glaciation occurred. This means that the homogeneously glaciating
144 filaments in these clouds were feeding the anvils with frozen cloud drops, which are distinctly
145 smaller than the ice particles that rise into the anvils within a heterogeneously glaciating cloud.
146 In summary, there are three types of anvil compositions, caused by three glaciation mechanisms
147 of the convective elements: (1) Large ice particles formed by heterogeneous glaciation; (2)
148 homogeneous glaciation of LWC that was generated at low levels in the cloud, and, (3)
149 homogeneous glaciation of newly nucleated cloud drops near or above the -38°C isotherm level
150 This third mechanism occurs mostly in cirrocumulus or in high wave clouds, as shown in Fig.
151 7a in Rosenfeld and Woodley, 2003). The manifestations of the first two mechanisms in the
152 composition of anvils are evident in the satellite analysis of cloud top temperature (T) versus
153 cloud top particle effective radius (r_e) shown in Fig. 1. In this red-green-blue composite brighter
154 visible reflectance is redder, smaller cloud top particles look greener, and warmer thermal

155 brightness temperature is bluer. This analysis methodology (Rosenfeld and Lensky, 1998) is
156 reviewed in Section 2.2 of this paper. The large ice particles formed by heterogeneous
157 glaciation appear red in Fig. 1 and occur at cloud tops warmer than the homogeneous glaciation
158 temperature of -38°C. The yellow cloud tops in Fig. 1 are colder than -38°C and are composed
159 of small ice particles that probably formed by homogeneous glaciation. The homogeneously
160 glaciated cloud water appeared to have ascended with the strongest updrafts in these clouds and
161 hence formed the tops of the coldest clouds.

162 The homogeneous freezing of LWC generated at low levels in convective clouds is of
163 particular interest here, because it is indicative of updrafts that are sufficiently strong such that
164 heterogeneous ice nucleation would not have time to deplete much of the cloud water before
165 reaching the homogeneous glaciation level. As such, the satellite signature in the form of
166 enhanced 3.7- μ m reflectance can be used as an indicator of the occurrence of strong updrafts,
167 which in turn are conducive to the occurrence of severe convective storms. This realization
168 motivated Lindsey et al. (2006) to look for anvils with high Geostationary Operational
169 Environmental Satellite (GOES) 3.9- μ m reflectance as indicators of intense updrafts. They
170 showed that cloud tops with 3.9- μ m reflectance $> 5\%$ occurred for $\tau < 100$ s, where τ is the
171 parameterized cloud drop residence time in the updraft between cloud base and the -38°C
172 isotherm level. Lindsey et al. (2006) calculated τ according to eq. 1:

173

$$\tau = D_{LCL/-38} / w_{max} \quad (1)$$

174 where

175

$$w_{max} = (2 \text{ CAPE})^{0.5} \quad (2)$$

176

177 and $D_{LCL/-38}$ is the distance [m] between the LCL and the -38°C isotherm level. The requirement
178 for $\tau < 100$ s for homogeneous glaciation can be contrasted with the in situ aircraft observations
179 of glaciation time of about 7 minutes at temperatures of -32°C to -35°C (Rosenfeld and
180 Woodley, 2000). This reflects the fact that actual updraft velocities are much smaller than w_{max} .

182 The concept of "residence time" fails for clouds that have warm bases, because even
183 with CAPE that is conducive to severe storms heterogeneous freezing is reached most of the
184 times. This is manifested by the fact that clouds with residence times less than 100 s and hence
185 with 3.9- μ m reflectivities greater than 5%, were almost exclusively west of about 100°W,
186 where cloud base heights become much cooler and higher (Lindsey, personal communications
187 pertaining to Figure 7 of his 2006 paper).

188 Aerosols play a major role in the determination of the vertical profiles of cloud
189 microstructure and glaciation. Khain et al. (2001) simulated with an explicit microphysical

190 processes model the detailed microstructure of a cloud that Rosenfeld and Woodley (2000)
191 documented, including the homogeneous glaciation of the cloud drops that nucleated near cloud
192 base at a temperature of about 9°C. When changing in the simulation from high to low
193 concentrations of CCN, the cloud drop number concentration was reduced from 1000 to 250
194 cm⁻³. Coalescence quickly increased the cloud drop size with height and produced
195 hydrometeors that froze readily and scavenged almost all the cloud water at -23°C, well below
196 the homogeneous glaciation level. This is consistent with the findings of Stith et al. (2004), who
197 examined the microphysical structure of pristine tropical convective clouds in the Amazon and
198 at Kwajalein, Marshall Islands. They found that the updrafts glaciated rapidly, most water being
199 removed between -5 and -17°C, and suggested that a substantial portion of the cloud droplets
200 were frozen at relatively warm temperatures.

201 In summary, the occurrence of anvils composed of homogeneously glaciated cloud
202 drops is not a unique indicator of intense updrafts, because it depends equally strongly on the
203 depth between cloud base and the -38°C isotherm level. The microphysical evolution of cloud
204 drops and hydrometeors as a function of height above cloud base reflects much better the
205 combined roles of aerosols and updrafts, with some potential of separating their effects. If so,
206 retrieved vertical microphysical profiles can provide us with information about the updraft
207 intensities. This will be used in the next section as the basis for the conceptual model of severe
208 storm microphysical signatures.

209

210 **2. A Conceptual Model of Severe Storm Microphysical Signatures**

211

212 **2.1 The vertical evolution of cloud microstructure as an indicator of updraft velocities 213 and CCN concentrations**

214

215 The vertical evolution of satellite-retrieved, cloud-top-particle, effective radius is used
216 here as an indicator of the vigor of the cloud. In that respect it is important to note that
217 convective cloud top drop sizes do not depend on the vertical growth rate of the cloud (except
218 for cloud base updraft), as long as vapor diffusion and condensation is the dominant cause for
219 droplet growth. This is so because: i) the amount of condensed cloud water in the rising parcel
220 depends only on the height above cloud base, regardless of the rate of ascent of the parcel, and
221 ii) most of cloud drops were formed near cloud base and their concentrations with height do not
222 depend on the strength of the updraft as long as drop coalescence is negligible.

223 The time for onset of significant coalescence and warm rain depends on the cloud drop
224 size. That time is shorter for larger initial drop sizes (Beard and Ochs, 1993). This time
225 dependency means also that a greater updraft would lead to the onset of precipitation at a
226 greater height in the cloud. This is manifested as a higher first precipitation radar echo height.
227 At supercooled temperatures the small rain drops freeze rapidly and continue growing by
228 riming as graupel and hail. The growth rate of ice hydrometeors exceeds significantly that of an
229 equivalent mass of rain drops (Pinsky et al., 1998). Conversely, in the absence of raindrops, the
230 small cloud drops in strong updrafts can remain liquid up to the homogeneous glaciation level
231 (Rosenfeld and Woodley, 2000). Filaments of nearly adiabatic liquid water content were
232 measured up to the homogeneous freezing temperature of -38°C by aircraft penetrations into
233 feeders of severe hailstorms with updrafts exceeding 40 ms^{-1} (Rosenfeld et al., 2006b). Only
234 very few small ice hydrometeors were observed in these cloud filaments. These feeders of
235 severe hailstorms produced 20 dBZ first echoes at heights of 8-9 km.

236 An extreme manifestation of strong updrafts with delayed formation of precipitation and
237 homogeneous glaciation is the echo free vault in tornadic and hail storms (Browning and
238 Donaldson, 1963; Browning, 1964; Donaldson, 1970), where the extreme updrafts push the
239 height for the onset of precipitation echoes to above 10 km. However, the clouds that are the
240 subject of main interest here are not those that contain the potential echo free vault, because the
241 vertical microstructure of such clouds is very rarely exposed to the satellite view. It is shown in
242 this study that the feeder clouds to the main storm and adjacent cumulus clouds possess the
243 severe storm satellite retrieved microphysical signature. The parallel to the echo free vault in
244 these clouds is a very high precipitation first echo height, as documented by Rosenfeld et al.
245 (2006b).

246 Although the role of updraft speed in the vertical growth of cloud drops and onset of
247 precipitation is highlighted, the dominant role of CCN concentrations at cloud base, as has been
248 shown by Andreae et al. (2004), should be kept in mind. Model simulations of rising parcels
249 under different CCN and updraft profiles were conducted for this paper to illustrate the
250 respective roles of those two factors in determining the relations between cloud composition,
251 precipitation processes and the updraft velocities. Although this parcel model (Pinsky and
252 Khain, 2002) has 2000 size bins and has accurate representations of nucleation and coalescence
253 processes, being a parcel prevents it from producing realistic widths of drop size distributions
254 due to various cloud base updrafts and supersaturation histories of cloud micro-parcels.
255 Therefore the calculations presented here can be viewed only in a relative qualitative sense.

256 A set of three updraft profiles (see Fig. 2) and four CCN spectra were simulated in the
257 parcel model. Cloud base updraft was set to 2 ms^{-1} for all runs. The maximum simulated drop
258 concentrations just above cloud base were 60, 173, 460 and 1219 cm^{-3} for the four respective
259 CCN spectra, denoted as CCN1 to CCN4 in Figs. 3 to 5. No giant CCN were incorporated,
260 because their addition results in a similar response to the reduction of the number
261 concentrations of the sub-micron CCN, at least when using the same parcel model (see Fig. 4 in
262 Rosenfeld et al., 2002). The dependence of activated cloud drop concentration on cloud base
263 updraft speed was simulated with the same parcel model (see Fig. 3). According to that, cloud
264 base updraft plays only a secondary role to the CCN in determining the cloud drop number
265 concentrations near cloud base.

266

267 Figure 4 shows that the updraft does not affect at all the cloud drop size below the
268 height of the onset of coalescence, which is the point where the lines of the various updrafts for
269 a given CCN diverge. The height of coalescence onset depends mainly on height and very little
270 on updraft speed. This is so because the coalescence rate is dominated by the size of the cloud
271 drops, which in turn depends only on cloud depth in the diffusional growth zone.

272 The updraft speed does affect the height of the onset of significant precipitation (H_R),
273 which is defined in Fig. 5 as rain water content / cloud water content =0.1. This is justified by
274 the remarkably consistent relations between CCN concentrations and vertical evolution of drop
275 size distribution up to the height of the onset of warm rain (H_R), as documented by Andreae et
276 al. (2004) and Freud et al. (2005). The sensitivity of H_R to a change of updraft from U1 to U3
277 can be quantified as H_R rising by 1000 m for CCN1, and by 3000 m for CCN4. The sensitivity
278 of H_R to change of CCN from CCN1 to CCN4 can be quantified as H_R rising by 2000 m for U1,
279 and by 4000 m for U3. Although the model does not simulate ice processes, these values are
280 still valid qualitatively for vigorous supercooled convective clouds (see for example Figs. 7 and
281 8 in Rosenfeld et al., 2006b), because the main precipitation embryos in such clouds come from
282 the coalescence process, except for clouds with unusually large concentrations of ice nuclei
283 and/or giant CCN.

284 This analysis shows that the vigor of the clouds can be revealed mainly by delaying the
285 precipitation processes to greater heights, and that the sensitivity becomes greater for clouds
286 forming in environments with greater concentrations of small CCN.

287

288 **2.2 Satellite inference of vertical microphysical profiles of convective clouds**

289

290 The vertical evolution of cloud top particle size can be retrieved readily from satellites,
291 using the methodology of Rosenfeld and Lensky (1998) to relate the retrieved effective radius
292 (r_e) to the temperature (T) of the tops of convective clouds. An effective radius $> 14 \mu\text{m}$
293 indicates precipitating clouds (Rosenfeld and Gutman, 1994). The maximum detectable
294 indicated r_e is $35 \mu\text{m}$, due to saturation of the signal. The T- r_e relations are obtained from
295 ensembles of clouds having tops covering a large range of T. This methodology assumes that
296 the T- r_e relations obtained from a snap shot of clouds at various stages of their development
297 equals the T- r_e evolution of the top of an individual cloud as it grows vertically. This
298 assumption was validated by actually tracking such individual cloud elements with a rapid
299 scanning geostationary satellite and comparing with the ensemble cloud properties (Lensky and
300 Rosenfeld, 2006).

301

302 Based on the shapes of the T- r_e relations (see Fig. 6), Rosenfeld and Lensky (1998)
303 defined the following five microphysical zones in convective clouds:

304

- 305 1) *Diffusional droplet growth zone*: Very slow growth of cloud droplets with depth above
306 cloud base, indicated by shallow slope of dr_e/dT .
- 307 2) *Droplet coalescence growth zone*: Large increase of the droplet growth rate dr_e/dT at T
308 warmer than freezing temperatures, indicating rapid cloud-droplet growth with depth
309 above cloud base. Such rapid growth can occur there only by drop coalescence.
- 310 3) *Rainout zone*: A zone where r_e remains stable between 20 and 25 μm , probably
311 determined by the maximum drop size that can be sustained by rising air near cloud top,
312 where the larger drops are precipitated to lower elevations and may eventually fall as
313 rain from the cloud base. This zone is so named, because droplet growth by coalescence
314 is balanced by precipitation of the largest drops from cloud top. Therefore, the clouds
315 seem to be raining out much of their water while growing. The radius of the drops that
316 actually rain out from cloud tops is much larger than the indicated r_e of 20-25 μm ,
317 being at the upper end of the drop size distribution there.
- 318 4) *Mixed phase zone*: A zone of large indicated droplet growth rate, occurring at $T < 0^\circ\text{C}$,
319 due to coalescence as well as to mixed phase precipitation formation processes.
320 Therefore, the mixed phase and the coalescence zones are ambiguous at $0 < T < -38^\circ\text{C}$.
321 The conditions for determining the mixed phase zone within this range are specified in
322 Rosenfeld and Lensky (1998).

323 5) *Glaciated zone*: A nearly stable zone of r_e having a value greater than that of the rainout
324 zone or the mixed phase zone at $T < 0^\circ\text{C}$.

325
326 All these microphysical zones are defined only for convective cloud elements. Multi-
327 layer clouds start with small r_e at the base of each cloud layer. This can be used to distinguish
328 stratified from convective clouds by their microstructure. Typically, a convective cloud has a
329 larger r_e than a layer cloud at the same height, because the convective cloud is deeper and
330 contains more water in the form of larger drops.

331
332 **2.3 T- r_e relations of severe convective storms in clouds with small drops**

333
334 A microphysically continental cloud is defined as such when CCN concentrations are
335 sufficiently large to induce a drop concentration that is sufficient to suppress drop coalescence
336 and warm rain in the lowest several (2 to 3) km of the cloud. According to Fig. 5 this translates
337 to drop concentrations greater than about 400 cm^{-3} near cloud base.

338 Even with small CCN concentrations, a sufficiently low cloud base temperature can
339 always be found such that the diffusional zone of cloud drops in the T- r_e line will extend
340 through the homogeneous glaciation temperature isotherm, even for moderate updraft
341 velocities. This is the case for many of the high plains storms over the western USA, as already
342 noted by Lindsey et al. (2006). This situation is represented schematically by line F of Fig. 7B.
343 Fig. 7 illustrates the T- r_e relations under various CCN and updraft scenarios according to the
344 conceptual model.

345 Alternatively, a cloud with an extremely large number of small droplets, such as in a
346 pyro-Cb (See example in Fig. 11 of Rosenfeld et al., 2006a), can occur entirely in the
347 diffusional growth zone up to the homogeneous glaciation level even if it does not have very
348 strong updrafts. In any case, a deep ($> 3 \text{ km}$) zone of diffusional growth is indicative of
349 microphysically continental clouds, where smaller r_e means greater heights and lower
350 temperatures that are necessary for the transition from diffusional to the mixed phase zone,
351 which is a manifestation of the onset of precipitation. This is demonstrated by the model
352 simulations shown in Figs. 4 and 5 here. Observations of such T- r_e relations in cold and high-
353 base clouds over New Mexico are shown in Fig. 1.

354 Fig. 7B illustrates the fact that a highly microphysically continental cloud with a warm
355 base (e.g., $> 10^\circ\text{C}$) has a deep zone of diffusional cloud droplet growth even for weak updrafts
356 (line A and Fig. 8a). The onset of precipitation is manifested as the transition to the mixed

357 phase zone, which occurs at progressively greater heights and colder temperatures for clouds
358 with stronger updrafts (line B and Fig. 8b). The glaciation temperature also shifts to greater
359 heights and colder temperatures with increasing updrafts. From the satellite point of view the
360 cloud is determined to be glaciated when the indicated r_e reaches saturation. This occurs when
361 the large ice crystals and hydrometeors dominate the radiative signature of the cloud. Some
362 supercooled water can still exist in such a cloud, but most of the condensates are already in the
363 form of large ice particles that nucleated heterogeneously and grew by riming and fast
364 deposition of water vapor that is in near equilibrium with liquid water. Such was the case
365 documented by Fridland et al. (2004) in convective clouds that ingested mid tropospheric CCN
366 in Florida, where satellite-retrieved T- r_e relations indicated a glaciation temperature of -29°C
367 (not shown).

368 Further invigoration of the clouds would shift upward the onset of mixed phase and
369 glaciated zones. But glaciation occurs fully and unconditionally at the homogeneous glaciation
370 temperature of -38°C. Any liquid cloud drops that reach to this level freeze homogeneously to
371 same-size ice particles. If most cloud water was not rimed on ice hydrometeors, it would have a
372 radiative impact on the retrieved effective radius and greatly decrease the r_e of the glaciated
373 cloud, as shown in line C of Fig. 7B. Yet additional invigoration of the updraft would further
374 shift upward and blur the onset of the precipitation, and reduce the r_e of the glaciated cloud
375 above the -38°C isotherm, until the ultimate case of the most extreme updraft, where the T- r_e
376 profile becomes nearly linear all the way up to the homogeneous freezing level. This situation
377 is illustrated by line E in Fig. 7A and 7B and in Figs. 8c-8e.

378

379 **2.4 T- r_e relations of severe convective storms in clouds with large drops**

380

381 Line A in Fig. 7A is similar to the scheme shown in Fig. 6, where a microphysically
382 maritime cloud with weak updrafts develops warm rain quickly and a rainout zone, followed by
383 a shallow mixed phase zone. When strengthening the updraft (line B), the time that is needed
384 for the cloud drops in the faster rising cloud parcel to coalesce into warm rain is increased.
385 Consequently, the rainout zone is reached at a greater height, but the onset of the mixed phase
386 zone is anchored to the slightly supercooled temperature of about -5°C. This decreases the
387 depth of the rainout zone. The greater updrafts push the glaciation level to colder temperatures.
388 Additional invigoration of the updraft (line C) eliminates the rainout zone altogether and further
389 decreases the glaciation temperature, thus creating a linear T- r_e line up to the glaciation
390 temperature. Even greater updrafts decrease the rate of increase of r_e with decreasing T, so that

391 the glaciation temperature is reached at even lower temperatures. It takes an extreme updraft to
392 drive the glaciation temperature to the homogeneous glaciation level, as shown in lines D and
393 observed in Fig. 8f.

394

395 Most cases in reality occur between the two end types that are illustrated schematically
396 in Fig. 7. Examples of $T-r_e$ lines for benign, hailing and tornadic convective storms are
397 provided in Fig. 8. It is remarkable that the $T-r_e$ relations occur not only in the feeders of the
398 main clouds, but also in the smaller convective towers in the area from which the main storms
399 appear to propagate (see figs. 8e and 8f). This does not imply that the smaller convective towers
400 and the upshear feeders have updraft speeds similar to the main storms, because these core
401 updrafts at the mature stage of the storms are typically obscured from the satellite view.
402 However, it does suggest that the satellite inferred updraft-related microstructure of those
403 smaller clouds and feeders is correlated with the vigor of the main updraft. This has
404 implications for forecasting, because the potential for severe storms can be revealed already by
405 the small isolated clouds that grow in an environment that is prone to severe convective storms
406 when the clouds are organized.

407 Based on the physical considerations above it can be generalized that a greater updraft is
408 manifested as a combination of the following trends in observable $T-r_e$ features:

- 409 • Glaciation temperature is reached at a lower temperature;
- 410 • A linear $T-r_e$ line occurs for a greater temperature interval;
- 411 • The r_e of the cloud at its glaciation temperature is smaller.

412

413 These criteria can be used to identify clouds with sufficiently strong updrafts to possess
414 a significant risk of large hail and tornadoes. The feasibility of this application is examined in
415 the next section.

416

417 **2.5 The roles of vertical growth rate and wind shear in measuring $T-r_e$ relations**

418

419 Severe convective storms often have updrafts exceeding 30 ms^{-1} . At this rate the air
420 rises 9 km within 5 minutes. The tops form anvils that diverge quickly, and without strong wind
421 shear the anvil obscures the new feeders to the convective storm, leaving a relatively small
422 chance for the satellite snap shot to capture the exposed tops of the vigorously growing
423 convective towers. Therefore, in a highly unstable environment with little wind shear the $T-r_e$
424 relations are based on the newly growing storms and on the cumulus field away from the

425 mature anviled storms. An example of moderate intensity little-sheared convection is shown in
426 Fig. 8a.

427 When strong wind shear is added, only strong and well organized updrafts can grow
428 into tall convective elements that are not sheared apart. The convective towers are tilted and
429 provide the satellite an opportunity to view from above their sloping tops and the vertical
430 evolution of their $T-r_e$ relations (see example in Figs. 8b and 8d). In some cases the strong
431 divergence aloft produces an anvil that obscures the upshear slope of the feeders from the
432 satellite view. Yet unorganized convective clouds that often pop up in the highly unstable air
433 mass into which the storm is propagating manage to grow to a considerable height through the
434 highly sheared environment and provide the satellite view necessary to derive their $T-r_e$
435 relations. Interestingly and importantly, the $T-r_e$ relations of these pre-storm clouds already
436 possess the severe storm microphysical signature, as evident in Fig. 8e. Without the strong
437 instability these deep convective elements would not be able to form in strong wind shear.
438 Furthermore, often some of the horizontal momentum diverts to vertical in a sheared convective
439 environment. Weisman and Klemp (1984) , modeling convective storms in different conditions
440 of vertical wind shear with directional variations, showed that updraft velocity is dependent on
441 updraft buoyancy and vertical wind shear. In strong shear conditions, the updraft of long-lived
442 simulated supercell storms interacted with the vertical wind shear, and this interaction resulted
443 in a contribution of up to 60% of the updraft strength. Furthermore, Brooks and Wilhelmson
444 (1990) showed, from numerical modeling experiments, an increased peak updraft speed with
445 increasing helicity. Therefore, the severe storm microphysical signature inherently incorporates
446 information about the wind shear and helicity.

447

448 **3.0 The Potential Use of the $T-r_e$ Relations for the Nowcasting of Severe Weather**

449

450 **3.1 Parameterization of the $T-r_e$ relations**

451

452 The next step was the quantitative examination of additional cases, taken from AVHRR
453 overpasses that occurred 0-75 minutes before the time of tornadoes and/or large hail in their
454 viewing area anywhere between the US east coast and the foothills of the Rocky Mountains.
455 The reports of the severe storms were obtained from the National Climate Data Center
456 (<http://www4.ncdc.noaa.gov/cgi-win/wwcgi.dll?wwEvent~Storms>). For serving as control
457 cases, visibly well defined non-severe storms (i.e., without reported tornado or large hail) were
458 selected at random from the AVHRR viewing areas. The control cases were selected from the
459 viewing area of the same AVHRR overpasses that included the severe convective storms at

460 distances of at least 250 km away from the area of reported severe storms. The relatively early
461 overpass time of the AVHRR with respect to the diurnal cycle of severe convective storms
462 allowed only a relatively small dataset from the years 1991-2001, the period in which the
463 NOAA polar orbiting satellites drifted to the mid and late afternoon hours. Unfortunately this
464 important time slot has been neglected since that time. In all, the dataset includes 28 cases with
465 tornadoes and hail, 6 with tornadoes and no hail, 24 with hail only and 38 with thunderstorms
466 but no severe weather. The case total was 96. The total dataset is given in Appendix A.

467 The AVHRR imagery for these cases was processed to produce the $T-r_e$ relations, using
468 the methodology of Rosenfeld and Lensky (1998). The $T-r_e$ functions were parameterized
469 using a computerized algorithm into the following parameters, as illustrated in Fig. 9:

470 Tbase: Temperature of cloud base, which is approximated by the warmest point of the $T-r_e$
471 relation.

472 Rbase: The r_e at cloud base.

473 T14: Temperature where r_e crosses the precipitation threshold of 14 μm .

474 TL: Temperature where the linearity of the $T-r_e$ relation ends upwards.

475 DTL: Temperature interval of the linear part of the $T-r_e$ relation. Tbase - TL

476 Tg: Onset temperature of the glaciated zone.

477 Rg: r_e at Tg.

478

479 These parameters provide the satellite inferences of cloud-base temperature, the
480 effective radius at cloud base, the temperature at which the effective radius reached the
481 precipitation threshold of 14 microns, the temperature at the top of the linear droplet growth
482 line and the temperature at which glaciation was complete. The $T-r_e$ part of the cloud which is
483 dominated by diffusional growth appears linear, because the non linear part near cloud base is
484 truncated due to the inability of the satellite to measure the composition of very shallow parts of
485 the clouds. The $T-r_e$ continues to be linear to greater heights and lower temperatures for more
486 vigorous clouds, as shown schematically in Fig. 7.

487 These parameters were retrieved for various percentiles of the r_e for a given T . The r_e at
488 a given T increases with the maturation of the cloud or with slower updrafts, especially above
489 the height for the onset of precipitation, as evident in Fig. 4. Therefore, characterization of the
490 growing stages of the most vigorous clouds requires using the small end of the distribution of r_e
491 for any given T . Fig. 10 shows the sensitivity of the parameterized $T-r_e$ properties of the
492 selected percentile for the calculation, for the percentiles, of 5, 10, 15,... 50. In order to avoid
493 spurious values, the 15th percentile and not the lowest was selected for the subsequent analyses.

494 The 15th percentile was used because it represents the young and most vigorously growing
495 convective elements, whereas larger percentiles represent more mature cloud elements. The
496 master table for the parameters at the 15th percentile for the convective areas and for the severe
497 storm reports of each case is provided in the Appendix.

498
499 The mean results by parameter and storm type are given in Table 1. According to the
500 table, the likelihood of a tornado is greater for a colder top of the linear zone and for a colder
501 glaciation temperature. In extreme cases such as that shown in Fig. 8e there is little difference
502 between Tg and TL because of what must have been violent updrafts. In addition, smaller
503 effective radius at cloud base indicates higher probability for a tornadic event.

504

505 **3.2 Statistical evaluation using AVHRR**

506

507 The primary goal of this section is to establish whether the probability of a tornado or
508 hail event might be quantified using the parameterized values of satellite retrieved T-r_e relations
509 of a given field of convective clouds. Doing this involved the use of binary logistic regression,
510 (Madalla, 1983), which is a methodology that provides the probability of the occurrence of one
511 out of two possible events.

512

513 If the probability of the occurrence of a tornado event is P, the probability for a non-
514 tornado is 1-P. Given predictors X₁, X₂,... X_i, the probability P of the tornado is calculated
515 using binary logistic regression with the predictors as continuous, independent, input variables
516 using equation (1):

517

$$(1) \ln\left(\frac{P}{1-P}\right) = \alpha + \beta x$$

518

519 Note that the basic model is similar in form to linear regression model (Note the right
520 side of the equation.), where α is the model constant and β is a coefficient of the parameter x of
521 the model. When doing binary logistic regression using multiple parameters or predictors,
522 equation (1) takes the form of equation (2):

523

$$(2) \ln\left(\frac{P}{1-P}\right) = \sum_i^n \alpha + \beta_i x_i = \alpha + \beta_1 x_1 + \beta_2 x_2 \dots + \beta_n x_n$$

524

525 Equation (2) means the following:

526

527

$$(3) \left(\frac{P}{1-P}\right) = \exp\left(\sum_i^n \alpha + \beta_i x_i\right) = \exp(\alpha + \beta_1 x_1 + \beta_2 x_2 \dots + \beta_n x_n)$$

528

$$(4) \frac{1-P}{P} = \frac{1}{P} - 1 = \exp\left(-\sum_i^n \alpha + \beta_i x_i\right) = \exp(-\alpha - \beta_1 x_1 - \beta_2 x_2 - \dots - \beta_n x_n)$$

530

$$(5) \frac{1}{P} = 1 + \exp\left(-\sum_i^n \alpha + \beta_i x_i\right) = 1 + \exp(-\alpha - \beta_1 x_1 - \beta_2 x_2 - \dots - \beta_n x_n), \text{ and finally}$$

532

$$(6) P = \frac{1}{1 + \exp\left(-\sum_i^n \alpha + \beta_i x_i\right)} = \frac{1}{1 + \exp(-\alpha - \beta_1 x_1 - \beta_2 x_2 - \dots - \beta_n x_n)}$$

534

535

536

537 The first step is calculation of P/(1-P) according to (3). The logistic regression was done
 538 in a stepwise fashion, so that the procedure was allowed to select the parameters that had the
 539 best predictive skill. Upon applying the regression procedures for the determination of the
 540 probability of a severe weather event as opposed to a less severe weather event (e.g., tornadoes
 541 and hail vs. none), the results shown in Table 2 were obtained. The left column of the table
 542 gives the modeled variable (e.g., None vs. Tornado) and the rows give the regression constants,
 543 their standard error and statistical significance (** = <0.01 and * = <0.05) corresponding to
 544 each indicated independent variable.

545

546 To illustrate how this might work, suppose one wanted to know in a given situation the
 547 probability that tornadoes are going to occur as opposed to none. From the table we can use
 548 either (A) Rbase, Tbase and Tg, where

549 $\alpha = 1.922, \beta_1 = -0.633, \beta_2 = -0.143$ and $\beta_3 = -0.156$.

550 or (B) Rbase, T14 and TL, where

551 $\alpha = -1.217, \beta_1 = -0.441, \beta_2 = -0.08$ and $\beta_3 = -0.144$.

552 For example, upon application of (B), if one lets $X_1 = 4 \mu\text{m}$, $X_2 = -20^\circ\text{C}$ and $X_3 = -36^\circ\text{C}$, then P
 553 $= 1/\{1 + \exp[1.217 + 0.441*4 + 0.08*(-5) + 0.144*(-10)]\} = 0.98$. Thus, given the input X
 554 values the probability of the tornadic event vs. None is highly probable.

555

556 This analysis can serve only as an illustration in which the same sample used to derive
 557 the relationships was used to test the relationships. An independent data set must be used to
 558 obtain a valid test of the value of the methodology in nowcasting severe weather events.
 559 Unfortunately, the small data sample that could be obtained does not allow having an
 560 independent dataset for this study. This should be, therefore, a subject of a subsequent study.

561
562 According to Fig. 11, it can be stated for this sample dataset that a tornadic storm can be
563 distinguished from a non-severe storm (NvsT) by having smaller Rbase with lower T14 and Tg.
564 This means that microphysical continentality along with slow vertical development of
565 precipitation in the clouds appear to be essential to the formation of tornadoes. Also non-
566 tornadic hail storms can be distinguished from non severe storms (NvsH in Fig. 11) by their
567 microphysically continental nature, as manifested by smaller Rbase and cooler cloud bases.
568 However, the tornadoes differ mostly from hail-only storms (HvsT in Fig. 11) by having
569 smaller r_e aloft (lower T14), extending the linear part of the T- r_e relations to greater heights
570 (greater dTL) and glaciating at lower temperatures that often approach the homogeneous
571 freezing isotherm of -38°C (lower Tg). The freezing occurs at smaller r_e (lower Rg). All this is
572 consistent with the conceptual model that is illustrated in Fig. 7.

573

574 **3.3 Statistical evaluation using GOES**

575

576 The applicability of the method depends on the possibility of using it with geostationary
577 satellite measurements. The feasibility of using comparably low resolution Geostationary
578 Operational Environmental Satellite (GOES) for early detection of severe convective storms
579 was tested, and the results are presented in this section. In using the GOES data it was
580 necessary to trade the fine (1-km) spatial resolution obtainable from the polar orbiters once-per-
581 day for the degraded 4-km spatial resolution that is available in GOES multi-spectral images
582 every 15 to 30 minutes. The lower accuracy of the GOES data did not seem to have a
583 systematic error when compared to AVHRR. The main effect was losing the smaller sub-pixel
584 cloud elements, which were primarily the lower and smaller clouds. Therefore, cloud base
585 temperature could not be relied on quantitatively as in the AVHRR, so that the scenes were
586 divided into two indicated cloud base temperature classes at 15°C. The effectiveness of the
587 detection of linearity of the profiles and glaciation temperature was compromised to a lesser
588 extent, because the cloud elements were already larger than the pixel size when reaching the
589 heights of the highly supercooled temperatures. No quantitative assessment of the effect of the
590 resolution was done in this preliminary study beyond merely testing the skill of the T- r_e
591 retrieved parameters.

592

593 The analysis using GOES was done only for detecting tornadoes, because the AVHRR
594 analysis showed that the predictor parameters had more extreme values for tornadoes than for
595 hail. Using the GOES data for separating hail and tornadoes was left for future research.

596
597

598 Seventeen (17) days with past tornadic events were examined using conventional
599 weather data and archived, multi-spectral, GOES-10 imagery, which were obtained from the
600 Cooperative Institute for Research in the Atmosphere's (CIRA) satellite archive. For each case,
601 the area of interest was first identified by noting severe weather reports from the Storm
602 Prediction Center's (SPC) website. The chosen area typically encompassed at least 6 central
603 U.S. states, but was larger for the more extensive severe weather outbreaks. Data were obtained
604 beginning in the morning, usually around 1600 UTC, and extended to near sunset. Rapid scan
605 imagery was not analyzed, and only the regular 15 to 30 minute scans were used. The GOES
606 satellite imagery was analyzed using the $T-r_e$ profiles for multiple significant convective areas
607 within the field of view. The $T-r_e$ parameters as defined in Fig. 9 were calculated for each such
608 convective area. The GOES-retrieved r_e reached saturation at $40 \mu\text{m}$, instead of $35 \mu\text{m}$ for the
609 AVHRR. Other than that the $T-r_e$ parameters were calculated similarly.

611 On the 17 case days there were 86 analyzed convective areas, 37 of the 86 analyzed
612 areas had a total of 78 tornadoes. For the purposes of this analysis a tornadic scene is one in
613 which the tornado occurred within 90 minutes of the GOES satellite observation. A non-
614 tornadic scene is one in which no tornado occurred throughout the period of GOES
615 measurement studied for a given area of study. The remaining scenes, in which the satellite
616 measurements were made at times > 90 minutes from the time of the tornado, were excluded.
617 The satellite cases were separated to those with satellite retrieved cloud base temperature
618 $T_b > 15^\circ\text{C}$ and $T_b < 15^\circ\text{C}$, because the warm base clouds are not likely to produce $T_g < 40 \mu\text{m}$
619 even when having very strong updrafts. This is inferred from the relations that were found by
620 Lindsey et al. (2006) between reflective cloud tops at $3.9 \mu\text{m}$, CAPE and the distance between
621 cloud base and the -38°C isotherm.

622

623 The logistic regression was done in a stepwise fashion, so that the procedure was
624 allowed to select the parameters that had the best predictive skill. The satellite-based predictors
625 were found to be at least as good as the sounding-based predictors, although the two are only
626 loosely correlated. The logistic regression parameters and coefficients data for the soundings
627 and satellite retrieved parameters are provided in Table 3.

628 The graphical representation of the probability for a tornado is depicted best by the
629 transformation of P to $\log_{10}(P/(1-P))$. This transformation of P is used in the graphical display
630 because it is important to expand the scales near $P=0$ and $P=1$. The relation between P and
631 $\log_{10}(P/(1-P))$ is shown in Fig. 12. Histograms of $\log_{10}(P/(1-P))$ for the satellite-based logistic
632 regression prediction models are shown in Figure 13. Note that the regression predictions
633 provide good separation for the tornadic and non-tornadic cases in most instances.

634 The lead time from the geostationary satellite data can be assessed from plots such as
635 presented in Fig. 14, which shows cases of some of the most intense tornadoes in the data set,
636 where the satellite predictor rises some 90 minutes or even more before the actual occurrence of
637 the tornado. In many cases it manifests itself with the first clouds that reach the glaciation level.
638 Fig. 15 integrates in 30 minute bins the tornado probabilities with respect to the time of
639 occurrence for all the tornadic storms in the dataset. The figure shows that the P of the pre-
640 tornadic convective clouds exceeds 0.5 already 150 minutes before the occurrence of the
641 tornado, and increases to 0.7 at a lead time of 90 minutes. In comparison, the median P of the
642 non-tornadic storms, as shown in Fig. 16, was about 0.06.

643

644 **3.4 Statistical evaluation using soundings**

645

646 Thus, the sounding based and satellite-based predictors complement one another. The
647 sounding-based predictor identifies generally where the tornado risk is high and then the
648 satellite-based predictor can be used to focus on the clouds in the area of greatest risk to predict
649 when the severe-weather potential is about to be realized. Before combining the two in future
650 studies, here we examine the predictive skill of the soundings separately for the exact same
651 convective areas that have been assessed with the GOES-based prediction.

652 For each convective area that was analyzed based by GOES-retrieval of $T-r_e$ relations,
653 four near-storm environmental variables were obtained in every chosen sector: cloud-base
654 temperature, surface-6-km shear (WS), Convective Available Potential Energy (CAPE), and
655 storm-relative helicity (SRH). Archived upper-air and surface data were obtained from the
656 Meteorological Assimilation Data Ingest System (MADIS), then viewed on an Advanced
657 Weather Interactive Processing System (AWIPS) workstation. For every area of interest, the
658 upper-air sounding considered most representative of the near-storm environment was chosen,
659 for times just prior to convective initiation of the storms producing the severe weather. If
660 necessary, the boundary layer temperature and dew point were adjusted based on hourly surface
661 data. For example, if thunderstorms occurred halfway between Amarillo, TX , and Oklahoma

662 City , OK , at 2100 UTC, an 1800 UTC sounding from Norman , OK , may have been chosen
663 for analysis. The afternoon surface data in western Oklahoma would be monitored, and the
664 surface temperature and dew point corresponding to convective initiation would be used to
665 modify the 1800 UTC sounding accordingly. A surface parcel was then lifted, allowing the
666 computation of cloud-base temperature and CAPE. Surface-6-km shear and storm-relative
667 helicity were obtained from the wind profile of the nearest sounding. Since storm-relative
668 helicity is *very* sensitive to both assumed storm motion and low level winds, and since it can
669 vary tremendously over a short distance due to the presence of boundaries, our estimates are
670 considered rough and may contain large errors. However, our confidence in the accuracy of the
671 other three variables is high.

672 A “conventional” logistic regression quantified the probability for a tornado in the
673 satellite-detected convective areas as a function of the synoptic sounding-measured variables
674 (i.e., cloud-base temperature, CAPE, WS and SRH. As one would have expected those areas
675 with tornadoes had warmer cloud-base temperatures, greater CAPE and helicity values and
676 slightly greater wind shear in the layer 0 to 6 km than the areas without tornadoes. Thus, it
677 comes as no surprise that the synoptic variables can be used to predict a general regional threat
678 of tornadoes, as has been already done in previous studies (e.g., Hamill and Church, 2000;
679 Dupilka et al., 2006a and 2006b; Davis, 2006). For a maximum similarity with the satellite
680 analysis, the sounding analysis was done separately for satellite-derived cloud base temperature
681 $Tb > 15^{\circ}\text{C}$ and $Tb < 15^{\circ}\text{C}$. The logistic regression parameters that were selected in the stepwise
682 procedure and their coefficients are provided in Table 3. Histograms of $\log_{10}(P/(1-P))$ for the
683 radiosonde and satellite-based predictors are shown in Figure 14.

684

685 **3.5 Comparison between the satellite and sounding predictors**

686

687 An overview of the performance of the sounding and satellite-derived predictive models
688 in separating the tornado and non-tornado cases is provided by the “box and whisker” plots for
689 the predictions of $\log_{10}(P/(1-P))$ from the prediction models (Figure 16). The left panel is for
690 the satellite combined predictor (using the appropriate predictor based on cloud base
691 temperature being above or below the 15°C threshold). The right panel is the predictor based on
692 the sounding alone. The bottom of each box is the 1st quartile value, the middle dark line
693 through the box is the median and the top is the 3rd quartile value. The bottom and top of each
694 whisker are the 5th and 95th percentiles, respectively. The more extreme values are given by the
695 individual circles.

696 The overall predictive skill of the soundings and the GOES satellite are comparable, but
697 the satellite is much more focused in time and space. The difference between the sounding and
698 satellite based predictions can be better understood when plotting the time dependent predictors
699 for tornadic cases, as shown in the examples in Figure 14. The sounding based predictor is
700 fixed in time and space for the analyzed area, because there is only one relevant sounding that
701 can indicate the pre-storm environment before the convective overturning masks it. The
702 satellite predictor on the other hand varies and is recalculated independently for each new
703 satellite observation. This allows the satellite based predictor to react to what the clouds are
704 actually doing as a function of time at scales that are not resolved properly by the soundings or
705 by models such as the Rapid Update Cycle (RUC).

707

708 **4.0 Discussion**

709

710 Based on the simulations here (Figs. 4 and 5) and their conceptual interpretations (Fig.
711 7), it can be stated that the microstructure of the lower parts of the clouds is dominated by the
712 aerosols, whereas the microstructure of the upper portions is dominated by the updraft
713 velocities. There are interactions between the two, where greater microphysical continentality
714 at the low levels, which might be caused by enhanced concentrations of small CCN aerosols,
715 would invigorate the updrafts in the clouds (Rosenfeld, 2006 and references therein). Clouds
716 with strong updrafts, having small initial effective radii, will be slow to develop precipitation,
717 virtually assuring that the updraft can continue unabated without the suppressive effects of
718 disruptive showers and downdrafts, which are displaced well downwind of the updraft core by
719 the shearing winds. This also means that tornadoes and large hail would be less probable in
720 microphysically maritime clouds, which develop in pristine air masses. On the other hand, this
721 hypothesis predicts that urban air pollution should increase the likelihood of severe storms,
722 which have been attributed so far mainly to heat island effects. The simulations of Van den
723 Heever and Cotton (2007) lend some support to this suggestion. This hypothesis requires
724 validation in additional research.

725

726 The association between strong updrafts, as inferred by the $T-r_e$ profiles, and hailstorms
727 makes sense physically. The combined physical considerations and preliminary statistical
728 results suggest that clouds with extreme updrafts and small effective radii are highly likely to
729 produce tornadoes and large hail, although the strength and direction of the wind shear
730 probably would be major modulating factors . The generation of tornadoes often (but not

731 always) requires strong wind shear in the lowest 6 km and low level helicity (Davis, 2006).
732 According to the satellite inferences here this might be helping spin up the tornadoes in storms
733 with very strong and deep updrafts that reach the anvil level. These strong updrafts aloft are
734 revealed by the linear $T-r_e$ profiles that extend to greater heights and r_e reaching smaller values
735 at the -38°C isotherm in tornadic versus hail storms. These inferred stronger and deeper
736 updrafts in tornadic storms compared to hailstorms imply that in low CAPE and high shear
737 environment some of the energy for the updrafts comes from converting horizontal to vertical
738 momentum, as already shown by Browning (1964). Fortuitously, the tilting of the feeder and
739 pre-storm clouds in the high shear tornadic storms render them easier to see by satellite and this
740 facilitates the derivation of the $T-r_e$ profiles and the retrieval of tornadic microphysical
741 signature, as described above.

742

743 This study is not aimed at testing (yet) an operational methodology for satellite
744 quantification of the risks of severe convective storms, but rather the testing of the validity of
745 the conceptual model that will hopefully allow subsequent development of such an operational
746 methodology using geostationary satellites. Therefore, the statistical analyses are exploratory in
747 nature at this stage of the research. Although the small sample size does not allow a rigorous
748 evaluation of the predictive skill of the conceptual model, it is sufficient to support the
749 conceptual model. The existence of the severe storm signature in the pre-storm clouds provides
750 us with the prospect that this methodology, when applied to geostationary multispectral satellite
751 imagery, will make it possible to identify earlier than is possible now developing cloud areas
752 that are about to become severe convective storms, possibly producing tornadoes and large hail.
753 The clouds in this early stage typically have not yet developed radar severe storm signatures.
754 Therefore, the capability of detecting the potential of clouds to become severe convective
755 storms may provide additional lead time for more focused "watch" areas, although with lesser
756 accuracy and focus than the detection of severe weather that is already possible with radar. This
757 method has the potential of filling the currently large gap between large, poorly focused
758 "watch" areas and "warnings" of severe convective storms that are actually observed
759 subsequently.

760
761
762
763
764

765 **5.0 Conclusions**
766

767 This research to date indicates that the potential of new growing deep convective clouds
768 to become storms that produce large hail and tornadoes can be revealed by the satellite-
769 retrieved vertical evolution of the microstructure of these clouds. Deep clouds composed of
770 small drops in their lower parts and cool bases are likely to produce hail, because such clouds
771 produce little warm rain and most of the condensate becomes supercooled water with relatively
772 small concentrations of precipitation embryos. Large graupel and small hail can develop under
773 such conditions. The hail becomes larger with greater updraft velocities at the supercooled
774 levels. This can be inferred by the increased depth of the supercooled zone of the clouds, as
775 indicated by lower glaciation temperatures. This is also manifested by an increase of the height
776 for onset of significant precipitation, as indicated by lower T14. Tornadic storms, which are
777 often accompanied by very large hail, are characterized by the parameters that indicate the
778 strongest updrafts at the supercooled levels, which are indicated by markedly lower values of
779 Tg and TL and smaller Rg than for hail-only storms.

780 The observations suggest that large concentrations of small aerosols might contribute to
781 the vigor of the storms, and to an increased likelihood of hail and tornadic storms. The severe
782 storm signature is an extensive property of the clouds that develop ahead of the actual hail or
783 tornadic storm clouds, suggesting that the probabilities of large hail and tornadoes can be
784 quantified at lead times of about 90 minutes or more.

785 This study does not address the role of wind shear in tornado development. However,
786 the extent that wind shear modulates severe storms by affecting their updraft speeds can be
787 revealed by the methodology presented in this study. The helicity of the wind shear should
788 increase the probability of a tornado for a given updraft velocity (Weisman and Klemp, 1984;
789 Brooks and Wilhelmson 1990; Rasmussen and Blanchard, 1998). A combination of the satellite
790 methodology with soundings parameters should be more powerful than each method alone. The
791 sounding and synoptic parameters identify the general areas at risk of severe weather and the
792 continuous multispectral satellite imagery identifies when and where that risk is about to be
793 realized.

794

795 This study suggests that multispectral satellite data have yet untapped predictive skill
796 for nowcasting of hail and mainly tornadic storms. This application will require using retrieved
797 microstructure from geostationary satellites, which provide smaller spatial resolution (3 to 4 km
798 at the sub geostationary satellite point) than the polar-orbiting satellites used in this study (1.1

799 km beneath the satellite) and are hence less useful. However, the added dimension of time
800 evolution that is possible with GOES imagery appears to compensate for its poorer spatial
801 resolution, and allows timely nowcasts of the risk of tornadoes from the developing storm
802 clouds. The development and testing of this method in an operational environment is now
803 underway by the authors of this paper.

804 While this method appears to have useful results with the current GOES satellites, it is
805 developed with the expectation of improved resolution with the next generation of
806 geostationary satellites. The resolution will be 2 km for the GOES-R and 1-km for the high
807 resolution coverage of the METEOSAT third generation.

808

809 **Acknowledgements**

810

811 The views, opinions, and findings in this report are those of the authors, and should not
812 be construed as an official NOAA and or U.S. Government position, policy, or decision.

813 **References**

814

815 Adler R.F., M.J. Markus, D.D. Fenn, 1983: Detection of severe Midwest thunderstorms using
816 geosynchronous satellite data. *Mon. Wea. Rev.*, **113**, 769-781.

817

818 Andreae M. O., D. Rosenfeld, P. Artaxo, A. A. Costa, G. P. Frank, K. M. Longo, and M. A. F.
819 Silva-Dias, 2004: Smoking rain clouds over the Amazon. *Science*, **303**, 1337-1342.

820

821 Beard K. V. and H. T. Ochs III, 1993: Warm-Rain Initiation: An Overview of Microphysical
822 Mechanisms. *Journal of Applied Meteorology*, **32**, 608-625.

823

824 Brooks H.E., J.W. Lee, J.P. Craven, 2003: The spatial distribution of severe thunderstorm and
825 tornado environments from global reanalysis data. *Atmospheric Research* **67– 68**, 73– 94.

826

827 Brooks, H. E., and R. B. Wilhelmson, 1990: The effect of low-level hodograph curvature on
828 supercell structure. Preprints, 16th Conf. on Severe Local Storms, Kananaskis Park, AB,
829 Canada, Amer. Meteor. Soc., 34–39.

830

831 Browning K.A., 1964: Airflow and precipitation trajectories within severe local storms which
832 travel to the right of the winds. *J. Atmos. Sci.*, **21**, 634-639.

833

834 Browning K.A., R.J. Donaldson Jr., 1963: Airflow and structure of a tornadic storm. *J. Atmos.*
835 *Sci.*, **20**, 533-545.

836

837 Davis J.M., 2006: Tornadoes in environments with small helicity and/or high LCL heights.
838 *Weather and Forecasting* **21**, 579-594.

839

840 Davies-Jones R.P., 1974: Discussion of measurements inside high-speed thunderstorm updrafts.
841 *J. Appl. Meteor.*, **13**, 710-717.

842

843 Donaldson R.J., 1970: Vortex Signature Recognition by a Doppler Radar. *Journal of Applied*
844 *Meteorology*, **9**, 661–670.

845

846 Dupilka M.L., G.W. Reuter, 2006a: Forecasting tornadic thunderstorm potential in Alberta
847 using environmental sounding data. Part I: Wind shear and buoyancy. *Weather and Forecasting*
848 **21**, 325-335.

849

850 Dupilka M.L., G.W. Reuter, 2006b: Forecasting tornadic thunderstorm potential in Alberta
851 using environmental sounding data. Part II: Helicity, precipitable water, and storm
852 convergence. *Weather and Forecasting* **21**, 336-346.

853

854 Hamill T.M., A.T. Church, 2000: Conditional probabilities of significant tornadoes from RUC-
855 2 Forecasts. *Weather and Forecasting* **15**, 461-475.

856

857 Freud E., Rosenfeld D., Meinrat O. Andreae ,Alexande A.Costa and Paulo Artaxo, 2005:
858 Observed robust relations between CCN and vertical evolution of cloud drop size distributions
859 in deep convective clouds. *Atmos. Chem. Phys. Discuss.*, **5**, 10155-10195.
860 <http://www.copernicus.org/EGU/acp/acpd/5/10155/acpd-5-10155.htm>

861
862 Fridlind, A. M., A. S. Ackerman, E. J. Jensen, A. J. Heymsfield, M. R. Poellot, D. E. Stevens,
863 D. Wang, L. M. Miloshevich, D. Baumgardner, R. P. Lawson, J. C. Wilson, R. C. Flragan, J. H.
864 Seinfeld, H. H. Jonsson, T. M. VanReken, V. Varatbangkul, and T. A. Rissman, 2004:
865 Evidence for the predominance of mid-tropospheric aerosols as subtropical anvil nuclei.
866 *Science*, **304**, 718-722.

867
868 Heymsfield, A. J., L. M. Miloshevich, C. Schmitt, A. Bansemer, C. Twohy, M. R. Poellot, A.
869 Fridlind, and H. Gerber, 2005: Homogeneous ice nucleation in subtropical and tropical
870 convection and its influence on cirrus anvil microphysics. *J. Atmos. Sci.*, **62**, 41–64.

871
872 Heymsfield G.M., G. Szejwach, S. Schotz, R.H. Blackmer Jr., 1983: Upper-level structure of
873 Oklahoma Tornadic storms on 2 May 1979. II: Proposed explanation of V pattern and internal
874 warm region in infrared observations. *J. Atmos. Sci.*, **42**, 1756-1767.

875
876 Jensen, E. J., and A. S. Ackerman (2006), Homogeneous aerosol freezing in the tops of high-
877 altitude tropical cumulonimbus clouds, *Geophys. Res. Lett.*, **33**, L08802,
878 doi:10.1029/2005GL024928.

879
880 Khain A. P., D. Rosenfeld and A. Pokrovsky, 2001: Simulating convective clouds with
881 sustained supercooled liquid water down to -37.5°C using a spectral microphysics model.
882 *Geophysical Research Letters*, **28**, 3887-3890.

883
884 Lensky I. M., D. Rosenfeld, 2006. The time-space exchangeability of satellite retrieved
885 relations between cloud top temperature and particle effective radius. *Atmos. Chem. Phys.* **6**,
886 2887-2894.

887
888 Levizzani, V., M. Setvák, 1996: Multispectral, high-resolution satellite observations of plumes
889 on top of convective storms. *J. Atmos. Sci.*, **53**, pp 361-369.

890
891 Lindsey D.T., D.W. Hillger, L. Grasso, J.A. Knaff, and J.F. Dostalek, 2006: GOES
892 Climatology and Analysis of Thunderstorms with Enhanced 3.9- μ m Reflectivity. *Monthly
893 Weather Review*, **134**, 2342-2353.

894
895 Madalla, G.S., 1983: Limited Dependent and Qualitative Variables in Econometrics, ISBN-13:
896 9780521241434, Cambridge Univ. Press, 416p.

897
898 McCann, D.W., 1983: The enhanced-V, a satellite observable severe storm signature. *Mon.
899 Wea. Rev.*, **111**, 887-894.

900
901 Pinsky, M. and Khain, A. P. 2002: Effects of in-cloud nucleation and turbulence on droplet
902 spectrum formation in cumulus clouds. *Q. J. R. Meteorol. Soc.*, **128**, 1–33.

903
904 Pinsky M. B., A. P. Khain, D. Rosenfeld, and A. Pokrovsky, 1998: Comparison of collision
905 velocity differences of drops and graupel particles in a very turbulent cloud. *Atmospheric
906 Research*, **49**, 99-113.

907
908 Rasmussen E.N., D.O. Blanchard, 1998: A baseline climatology of sounding-derived supercell
909 and tornado forecast parameters. *Weather and Forecasting*, **13**, 1148-1164.

910

911 Rissman T.A., 2004: Evidence for the predominance of mid-tropospheric aerosols as
912 subtropical anvil nuclei. *Science*, **304**, 718-722.

913

914 Rosenfeld D. and G. Gutman, 1994: Retrieving microphysical properties near the tops of
915 potential rain clouds by multispectral analysis of AVHRR data. *Atmospheric Research*, **34**,
916 259-283.

917

918 Rosenfeld D., R. Lahav, A. P. Khain, M. Pinsky, 2002: The role of sea-spray in cleansing air
919 pollution over ocean via cloud processes. *Science*, **297**, 1667-1670.

920

921 Rosenfeld D. and I. M. Lensky, 1998: Satellite-based insights into precipitation formation
922 processes in continental and maritime convective clouds. *The Bulletin of American
923 Meteorological Society*, **79**, 2457-2476.

924

925 Rosenfeld D. and W. L. Woodley, 2000: Deep Convective Clouds with Sustained Supercooled
926 Liquid Water Down to -37.5°C . *Nature*, **405**, 440-442.

927

928 Rosenfeld D. and W. L. Woodley, 2003: Closing the 50-year circle: From cloud seeding to
929 space and back to climate change through precipitation physics. Chapter 6 of "Cloud Systems,
930 Hurricanes, and the Tropical Rainfall Measuring Mission (TRMM)" edited by Drs. Wei-Kuo
931 Tao and Robert Adler, 234pp., p. 59-80, *Meteorological Monographs* **51**, AMS.

932

933 Rosenfeld D., 2006: Aerosol-Cloud Interactions Control of Earth Radiation and Latent Heat
934 Release. *Space Science Reviews*. Springer, 9p. 6 December 2006. DOI: 10.1007/s11214-006-
935 9053-6.
936 <http://dx.doi.org/10.1007/s11214-006-9053-6>

937

938 Rosenfeld D., M. Fromm, J. Trentmann, G. Luderer, M. O. Andreae, and R. Servranckx,
939 2006a: The Chisholm firestorm: observed microstructure, precipitation and lightning activity of
940 a pyro-Cb. *Atmos. Chem. Phys. Discuss.*, **6**, 9877–9906, 2006.

941

942 Rosenfeld D. and W. L. Woodley, 2003: Closing the 50-year circle: From cloud seeding to
943 space and back to climate change through precipitation physics. Chapter 6 of "Cloud Systems,
944 Hurricanes, and the Tropical Rainfall Measuring Mission (TRMM)" edited by Drs. Wei-Kuo Tao and Robert
945 Adler, 234pp., p. 59-80, *Meteorological Monographs* **51**, AMS.

946

947 Rosenfeld D., W. L. Woodley, T. W. Krauss, V. Makitov, 2006b: Aircraft Microphysical
948 Documentation from Cloud Base to Anvils of Hailstorm Feeder Clouds in Argentina. *J. Appl.
949 Meteor.*, **45**, 1261–1281, September 2006.

950

951 Setvák M., Rabin R.M., Doswell C.A., Levizzani V., 2003: Satellite observations of
952 convective storm top features in the 1.6 and 3.7/3.9 μm spectral bands. *Atmos. Research*, 67-
953 68C, 589-605.

954

955 Stith, J. L., J. A. Hagerty, A. J. Heymsfield, and C. A. Grainger, 2004: Microphysical
956 characteristics of tropical updrafts in clean conditions. *J. Appl. Meteor.*, **43**, 779-794.

957

958 Twomey S., 1959: The nuclei of natural cloud formation. II. The supersaturation in natural
959 clouds and the variation of cloud droplet concentrations. *Geofis. Pur Appl.*, 43, 243-249.
960

961 Van den Heever S.C., W.R. Cotton, 2007: Urban Aerosol Impacts on Downwind Convective
962 Storms. *J. Appl. Meteor. Clim.*, **46**, 828-850.
963

964 Weisman, M. L., and J. B. Klemp, 1984: The structure and classification of numerically
965 simulated convective storms in directionally varying wind shears. *Mon. Wea. Rev.*, 112, 2479–
966 2498.
967

Table 1: The mean and standard deviations of the $T-r_e$ parameters as defined in Fig. 9, for the various categories of the dataset. The Tornado column $F \geq 1$ is for the cases of tornadoes with a F scale of at least 1, with or without hail. The rest of the columns contain independent data that in all constitute the full dataset of $28+6+24+38=96$ cases. Each cell in the table contains the mean \pm the standard deviation.

	Tornado $F \geq 1$	Tornado +hail	Tornado only	Hail only	None
N	13	28	6	24	38
Hail size [""]	2.5 ± 1.2	2.1 ± 1.0		1.6 ± 0.9	
Tbase [°C]	13.2 ± 5.0	13.6 ± 4.7	13.3 ± 7.8	11.6 ± 5.3	15.7 ± 5.7
Rbase [μm]	5.2 ± 1.2	5.4 ± 2.3	7.2 ± 2.3	6.9 ± 1.6	7.8 ± 1.5
T14 [°C]	-17.6 ± 10.8	-14.5 ± 10.0	-8.8 ± 13.6	-12.6 ± 7.2	-4.4 ± 6.7
TL [°C]	-31.0 ± 5.1	-31.2 ± 6.4	-27.3 ± 7.5	-23.8 ± 8.4	-19.8 ± 9.6
dTL [°C]	44.2 ± 6.5	44.8 ± 7.9	40.7 ± 10.5	35.5 ± 10.2	35.6 ± 10.7
Tg [°C]	-33.5 ± 3.9	-33.9 ± 4.8	-29.5 ± 4.9	-28.8 ± 7.8	-25.7 ± 6.5
Rg [μm]	27.7 ± 6.4	27.5 ± 6.0	30.8 ± 5.4	31.9 ± 3.3	32.8 ± 2.5

Table 2: The parameters of the logistic regression for determining the probability of various categories of convective storms reaching severe status. The table contains the α and β coefficients \pm the standard errors of the T-r_e parameters in the logistic regression as expressed in Equation 2. Included are only the variables that were selected by the stepwise regression as statistically significant. The statistical significance is marked as *= <0.05 , **= <0.01 and ***= <0.001 . NS means not significant.

T - r _e Variable		Rbase	Tbase	T14	TL	Tg	Rg	dTL
Model Variable	α (sig.)	β (sig.)						
None vs. Tornado	1.922 (NS)	-0.633 (**)	-0.143 (*)			-0.156 (**)		
None vs. Tornado	-1.217 (NS)	-0.441 (*)		-0.080 (*)	-0.144 (**)			
None vs. Hail	10.376 (***)	-0.979 (**)	-0.261 (***)					
None vs. YES	5.648 (**)	-0.648 (***)	-0.174 (***)		-0.082 (**)			
None vs. YES	4.910 (*)	-0.611 (***)	-0.169 (**)			-0.082 (*)		
Hail vs. Tornado	5.727 (NS)			0.097 (*)		-0.146 (*)	-0.273 (**)	
Hail vs. Tornado	3.443 (NS)			0.038 (NS)			-0.194 (*)	0.089 (*)

Table 3: The parameters of the logistic regression models for P/I-P as calculated by (3)

GOES, Tb>15C, R ² =0.525	
Parameter	β
Tg	-0.204
Rg	-0.129
Rbase	0.415
Constant α	-5.725

GOES, Tb<15C, R ² =0.648	
Parameter	β
Tg	-0.249
Rg	-0.249
T14	0.114
Constant α	0.092

Radiosonda, Tb>15C, R ² =0.393	
Parameter	β
Helicity	0.005
CAPE	0.001
Constant α	-2.424

Radiosonda, Tb<15C, R ² =0.387	
Parameter	β
T Cloud Base	-0.304
Shear 0-6 km	0.038
CAPE	0.001
Constant α	-3.433

Figure Captions

Figure 1: A $T-r_e$ analysis of the cloud top microstructure of a Cb (cumulonimbus) that has an anvil partially formed by homogeneous freezing. The image is based on a NOAA-AVHRR overpass on 8 June 1998, 22:12 UTC over New Mexico. The domain is 220x150 AVHRR 1-km pixels. The image is an RGB composite where the visible channel modulates the red, $3.7\text{ }\mu\text{m}$ reflectance modulates the green, and $10.8\text{ }\mu\text{m}$ brightness temperature modulates the blue (after Rosenfeld and Lensky, 1998). Brighter $3.7\text{ }\mu\text{m}$ reflectance (greener) means smaller cloud top particles. The inset shows the $T-r_e$ lines for the clouds in the marked rectangle. The different colored lines represent different $T-r_e$ percentiles every 5% from 5% (left most line) to 100% (right most line), where the bright green is the median. The white line on the left side of the inset is the relative frequency of the cloudy pixels. The vertical lines show the vertical extent of the microphysical zones: yellow for the diffusional growth; green for the coalescence zone (does not occur in this case); pink for the mixed phase and red for the glaciated zone. The glaciated cloud elements that do not exceed the -38°C isotherm appear red and have very large r_e that is typical of ice particles that form by heterogeneous freezing in a mixed phase cloud, whereas the colder parts of the anvil are colored orange and are composed of small particles, which must have formed by homogeneous freezing of the cloud drops in the relatively intense updraft that was necessary to form the anvil portions above the -38°C isotherm.

Figure 2: The updraft profiles for the simulations presented in Figures 4 and 5. The updrafts are denoted as U1 to U3 from the weakest to the strongest.

Figure 3: The simulated dependence of cloud drop number concentrations on cloud base updraft for the CCN spectra used in the simulations of Figs. 4 and 5.

Figure 4: The simulated cloud drop effective radius as a function of height for various combinations of updraft profiles and cloud base drop concentrations. The updrafts are shown in Fig. 2, and the CCN create 60, 173, 460 and $1219\text{ drops cm}^{-3}$ at cloud base, for CCN1 to CCN4, respectively. The cloud base temperature is 20°C . Note the exclusive role of the CCN up to the height of the onset of coalescence, which is where, for a given CCN, the lines for the different updrafts separate.

Figure 5: Same as Fig. 4, but for the ratio of rain water content / cloud water content.

Figure 6: The classification scheme of convective clouds into microphysical zones, according to the shape of the $T-r_e$ relations (after Rosenfeld and Woodley, 2003). The microphysical zones can change considerably between microphysically continental and maritime clouds, as illustrated in Fig. 6 of Rosenfeld and Woodley, 2003.

Figure 7: A conceptual model of the way $T-r_e$ relations of convective clouds are affected by enhanced updrafts to extreme values. The vertical green line represents the precipitation threshold of $r_e=14 \mu\text{m}$ (Rosenfeld and Gutman, 1994). The horizontal line at $T=-38^\circ\text{C}$ represents the homogeneous freezing isotherm. The left panel is for microphysically maritime clouds with low and warm bases and small concentrations of CCN, and the right panel is for clouds with high CCN concentrations or high and cold bases. In reality most cases occur between these two end types.

Figure 8a: Same as Fig. 1, but for a non-severe convective storm. The image is based on the NOAA-AVHRR overpass on 28 July 1998, 20:24 UTC, over a domain of 232x222 AVHRR 1-km pixels. The cloud system is just to the north of the Florida Panhandle. Note the rapid increase of r_e towards an early glaciation at -17°C . This is case #9855 (see Appendix), with $T_{\text{base}}=20^\circ\text{C}$, $R_{\text{base}}=8 \mu\text{m}$, $T_{14}=-5^\circ\text{C}$, $TL=-18^\circ\text{C}$, $dTL=38^\circ\text{C}$, $T_g=-20^\circ\text{C}$, $R_g=33.5 \mu\text{m}$ (See parameter definitions in Fig. 9).

Figure 8b: Same as Fig. 1, but for three hail storms. The image is based on the NOAA-AVHRR overpass on 5 March 1999, 21:32 UTC, at a domain of 220x300 AVHRR 1-km pixels. The cloud system is near the eastern border of Oklahoma. The locations of reported hail (0.75-1.75 inch) are marked by small triangles. Note the deep supercooled layer with glaciation temperature of about -25 for the median r_e (denoted by the bottom of the vertical red line), and less than -30°C for the smallest r_e . This is case #9901 (see Appendix), with $T_{\text{base}}=8^\circ\text{C}$, $R_{\text{base}}=5 \mu\text{m}$, $T_{14}=-12^\circ\text{C}$, $TL=-26^\circ\text{C}$, $dTL=34^\circ\text{C}$, $T_g=-27^\circ\text{C}$, $R_g=32.4 \mu\text{m}$ (See parameter definitions in Fig. 9).

Figure 8c: Same as Fig. 1, but for tornadic storms. The image is based on the NOAA-AVHRR overpass on 29 June 1993, 22:03 UTC, over a domain of 251x210 AVHRR 1-km pixels. The cloud occurred in north central Nebraska. The locations of reported hail and tornadoes within

the hour of the image are marked by small triangles and rectangles, respectively. The north storm produced a F2 tornado at 21:49. Note the r_e remaining very small up to the homogeneous freezing temperature of -39°C . The scarcity of points in the interval of -14°C to -38°C disqualifies this case to be included in the analyses.

Figure 8d: Same as Fig. 1, but for a tornadic storm with 4.5 inch hail. The image is based on the NOAA-AVHRR overpass on 29 June 2000, 22:21 UTC, over a domain of 282x264 AVHRR 1-km pixels. The cloud occurred in southwestern Nebraska. The locations of a reported F1 tornado at 23:28 is marked by a rectangle. Note that the tornado occurred in a region that had little cloud development 68 minutes before the tornadic event. This demonstrates that there is predictive value in the cloud field before any of the clouds reach severe stature. A hail swath on the ground can be seen as the dark purple line emerging off the north flank of the storm, oriented NW-SE. Two hail gushes are evident on the swath near the edge of the storm. The precipitation swath appears as darker blue due to the cooler wet ground. Note the linear profile of the $T-r_e$ lines, and the glaciation occurs at the small $r_e=25 \mu\text{m}$, in spite of the very warm cloud base temperature near 20°C . This is case #0046 (see Appendix), with $T_{\text{base}}=8^\circ\text{C}$, $R_{\text{base}}=5.5 \mu\text{m}$, $T_{14}=-21^\circ\text{C}$, $TL=-31^\circ\text{C}$, $dTL=39^\circ\text{C}$, $T_g=-32^\circ\text{C}$, $R_g=20.6 \mu\text{m}$ (See parameter definitions in Fig. 9).

Figure 8e: Same as Fig. 1, but for a tornadic storm with 2.5 inch hail. The image is based on the NOAA-AVHRR overpass on 30 April 2000, 22:14 UTC, over a domain of 333x377 AVHRR 1-km pixels. The cloud occurred just to the SE of the Texas panhandle. The location of a reported F3 tornado at 22:40 is marked by a rectangle. Note the very linear profile of the $T-r_e$ lines, and the glaciation occurs at the small $r_e=25 \mu\text{m}$, in spite of the very warm cloud base temperature of near 20°C , as in Fig. 8d. It is particularly noteworthy that this $T-r_e$ is based on clouds that occurred ahead of the main storm into an area through which the storm propagated. The same is indicated in Fig. 8d, but to a somewhat lesser extent. This is case #0018 (see Appendix), with $T_{\text{base}}=18^\circ\text{C}$, $R_{\text{base}}=4.4 \mu\text{m}$, $T_{14}=-15^\circ\text{C}$, $TL=-37^\circ\text{C}$, $dTL=55^\circ\text{C}$, $T_g=-38^\circ\text{C}$, $R_g=23.9 \mu\text{m}$ (See parameter definitions in Fig. 9).

Figure 8f: Same as Fig. 1, but for a tornadic storm with 1.75 inch hail. The image is based on the NOAA-AVHRR overpass on 20 July 1998, 20:12 UTC, over a domain of 262x178 AVHRR 1-km pixels. The cloud occurred in NW Wisconsin. The locations of reported F0 tornadoes are

marked by rectangles. Note the large r_e at the lower levels, indicating microphysically maritime microstructure, followed by a very deep mixed phase zone. Very strong updrafts should exist for maintaining such a deep mixed phase zone in a microphysically maritime cloud, as illustrated in line C of Fig. 7A. This is case #9847 (see Appendix), with $T_{base}=16^\circ\text{C}$, $R_{base}=8 \mu\text{m}$, $T_{14}=8^\circ\text{C}$, $TL=-31^\circ\text{C}$, $DTL=47^\circ\text{C}$, $T_g=-32^\circ\text{C}$, $R_g=27.8 \mu\text{m}$ (See parameter definitions in Fig. 9).

Fig. 9: Illustration of the meaning of the parameters describing the $T-r_e$ relations.

T_{base} : Temperature of cloud base, which is approximated by the warmest point of the $T-r_e$ relation.

R_{base} : The r_e at cloud base.

T_{14} : Temperature where r_e crosses the precipitation threshold of 14 μm .

TL : Temperature where linearity of the $T-r_e$ relation ends upwards.

DTL : Temperature interval of the linear part of the $T-r_e$ relation. $T_{base} - TL$

T_g : Onset temperature of the glaciated zone.

R_g : r_e at T_g

Figure 10: Mean and standard error of the parameterized $T-r_e$ properties for the r_e percentiles of 5, 10, 15, ..., 50 for a given T , for tornadic, hail only and non-severe storms. Note the obvious increase of r_e at the base with higher percentile, and the decrease of R_{base} for more severe storms (A). Note the decrease in TL (B), T_g (C) and R_g (D) for the younger and more vigorous cloud elements as represented by the smaller percentiles and for the more severe storms.

Figure 11: The binary logistic regression probability of discriminating a tornado versus non severe convective storm (NvsT, red), a hail storm versus non severe storm (NvsH, blue) and a tornado versus hail-only storm (HvsT, green), and severe vs. non severe storms (NvsY, black). The probabilities for the various values of the $T-r_e$ parameters are calculated based on the coefficients in Table 2, when fixing the other parameters at their mean values.

Figure 12: The relations between the probability for an event P and the transformation to $\log_{10}(P/(1-P))$.

Figure 13: Histograms of the predictions $\log_{10}(P/(1-P))$ for the GOES satellite (A) and the sounding (B) based models. The upper panel is for tornadic scenes, and the lower panel for non tornadic areas.

Figure 14: The time dependence of the satellite (blue) and sounding (red) predictors for tornadoes when strong tornadoes occurred.

Figure 15: Box plots of the predictions $\log_{10}(P/(1-P))$ as a function of time relative to the time of tornado occurrence for the GOES satellite-combined prediction models (using the appropriate predictor based on cloud base temperature being above or below the 15°C threshold).

Figure 16: Box plots of the predictions $\log_{10}(P/(1-P))$ for the prediction models, for tornadic and non-tornadic storms. Zero means probability for a tornado $P=0.5$. The left panel is for the satellite prediction. The right panel is the predictor based on the sounding.

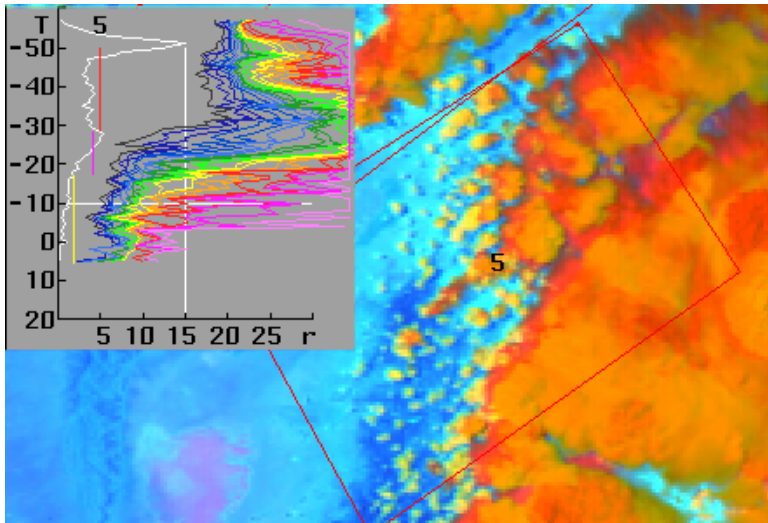


Figure 1: A $T-r_e$ analysis of the cloud top microstructure of a Cb (cumulonimbus) that has an anvil partially formed by homogeneous freezing. The image is based on a NOAA-AVHRR overpass on 8 June 1998, 22:12 UTC over New Mexico. The domain is 220x150 AVHRR 1-km pixels. The image is an RGB composite where the visible channel modulates the red, 3.7 μm reflectance modulates the green, and 10.8 μm brightness temperature modulates the blue (after Rosenfeld and Lensky, 1998). Brighter 3.7 μm reflectance (greener) means smaller cloud top particles. The inset shows the $T-r_e$ lines for the clouds in the marked rectangle. The different colored lines represent different $T-r_e$ percentiles every 5% from 5% (left most line) to 100% (right most line), where the bright green is the median. The white line on the left side of the inset is the relative frequency of the cloudy pixels. The vertical lines show the vertical extent of the microphysical zones: yellow for the diffusional growth; green for the coalescence zone (does not occur in this case); pink for the mixed phase and red for the glaciated zone. The glaciated cloud elements that do not exceed the -38°C isotherm appear red and have very large r_e that is typical of ice particles that form by heterogeneous freezing in a mixed phase cloud, whereas the colder parts of the anvil are colored orange and are composed of small particles, which must have formed by homogeneous freezing of the cloud drops in the relatively intense updraft that was necessary to form the anvil portions above the -38°C isotherm.

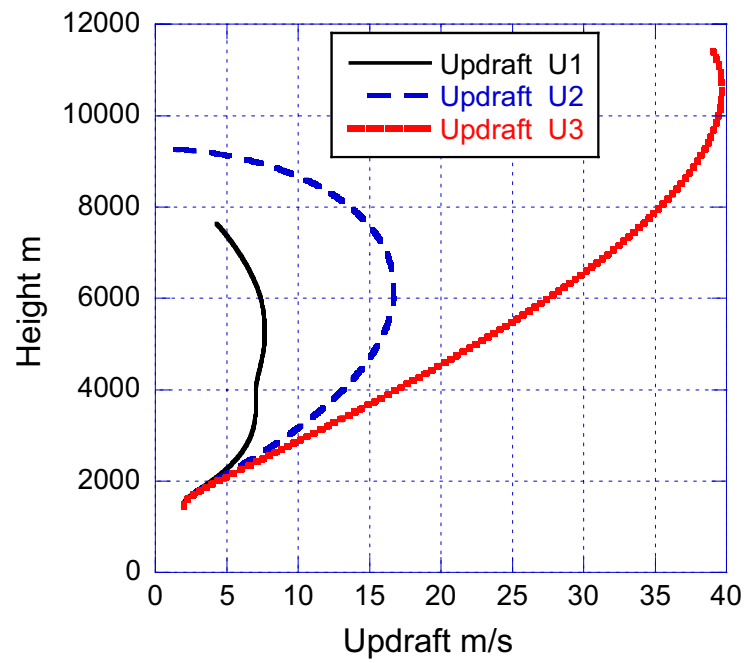


Figure 2: The updraft profiles for the simulations presented in Figures 4 and 5. The updrafts are denoted as U1 to U3 from the weakest to the strongest.

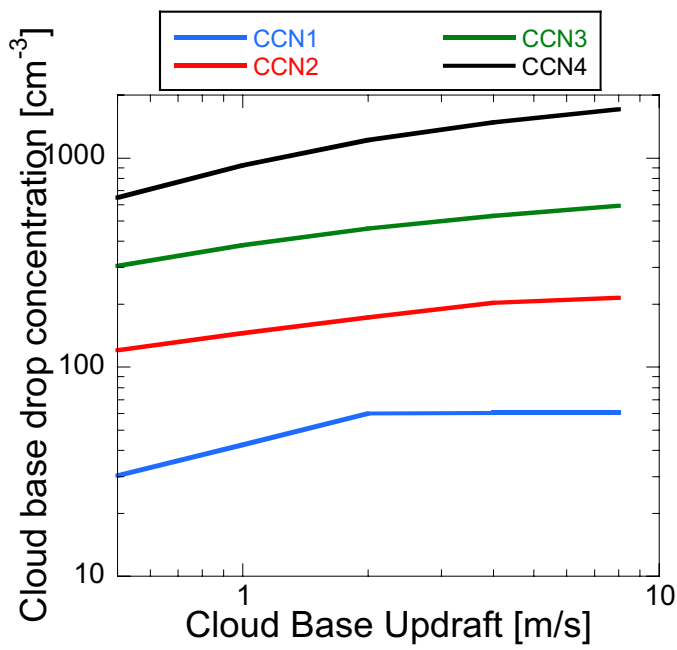


Figure 3: The simulated dependence of cloud drop number concentrations on cloud base updraft for the CCN spectra used in the simulations of Figs. 4 and 5.

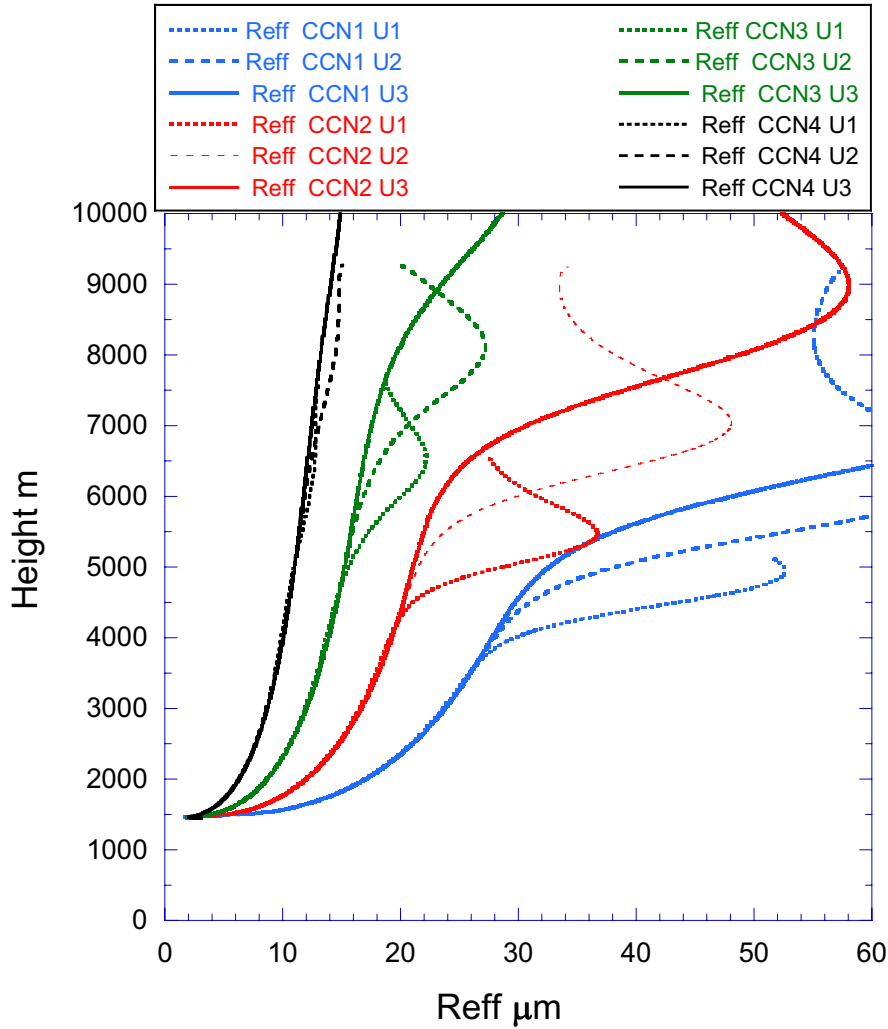


Figure 4: The simulated cloud drop effective radius as a function of height for various combinations of updraft profiles and cloud base drop concentrations. The updrafts are shown in Fig. 2, and the CCN create 60, 173, 460 and 1219 drops cm^{-3} at cloud base, for CCN1 to CCN4, respectively. The cloud base temperature is 20°C. Note the exclusive role of the CCN up to the height of the onset of coalescence, which is where, for a given CCN, the lines for the different updrafts separate.

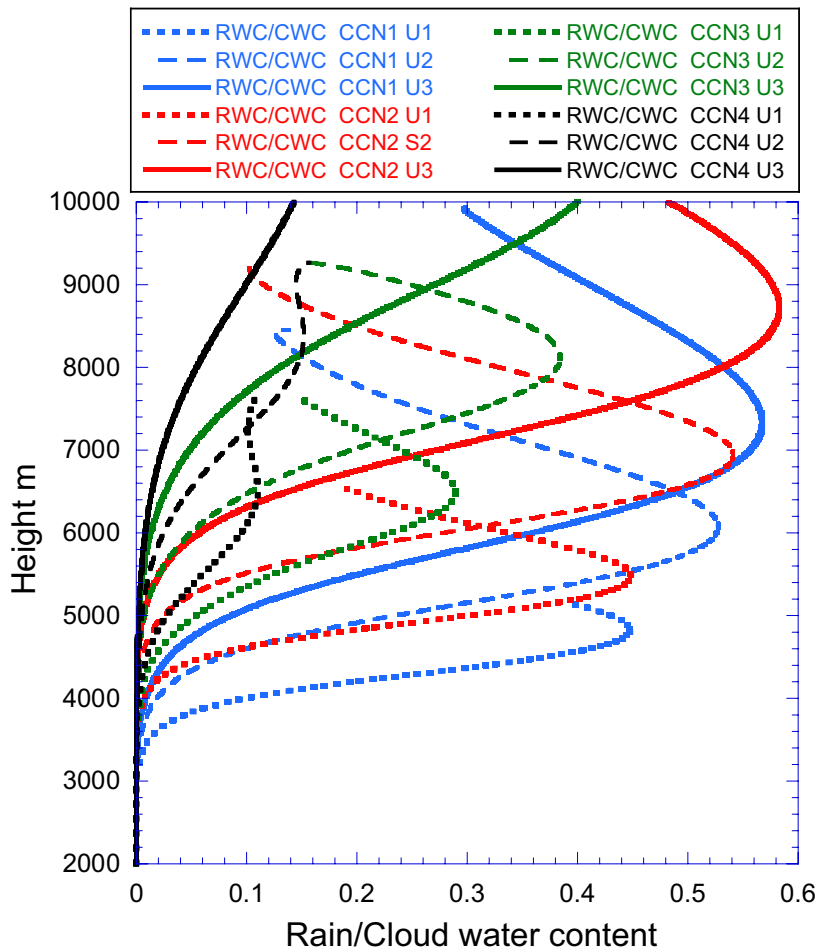


Figure 5: Same as Fig. 4, but for the ratio of rain water content / cloud water content.

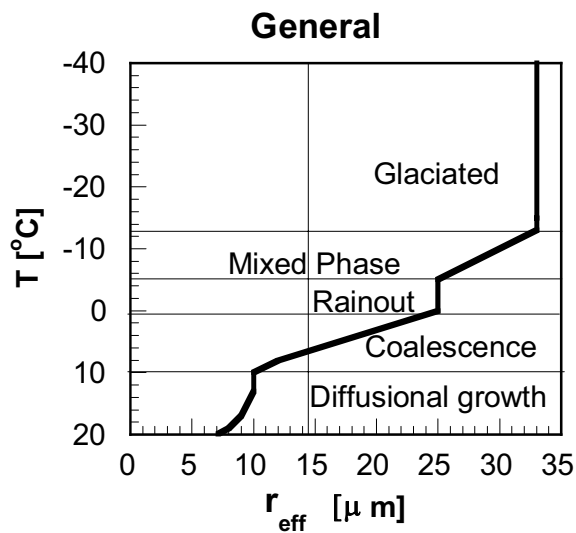


Figure 6: The classification scheme of convective clouds into microphysical zones, according to the shape of the $T-r_e$ relations (after Rosenfeld and Woodley, 2003). The microphysical zones can change considerably between microphysically continental and maritime clouds, as illustrated in Fig. 6 of Rosenfeld and Woodley, 2003.

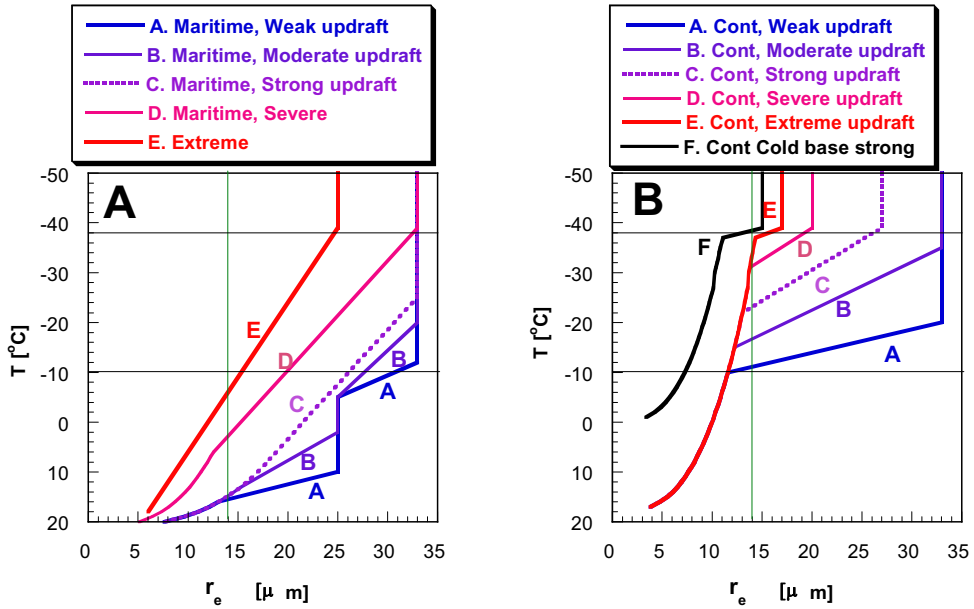


Figure 7: A conceptual model of the way $T-r_e$ relations of convective clouds are affected by enhanced updrafts to extreme values. The vertical green line represents the precipitation threshold of $r_e=14 \mu m$ (Rosenfeld and Gutman, 1994). The horizontal line at $T=-38^\circ C$ represents the homogeneous freezing isotherm. The left panel is for microphysically maritime clouds with low and warm bases and small concentrations of CCN, and the right panel is for clouds with high CCN concentrations or high and cold bases. In reality most cases occur between these two end types.

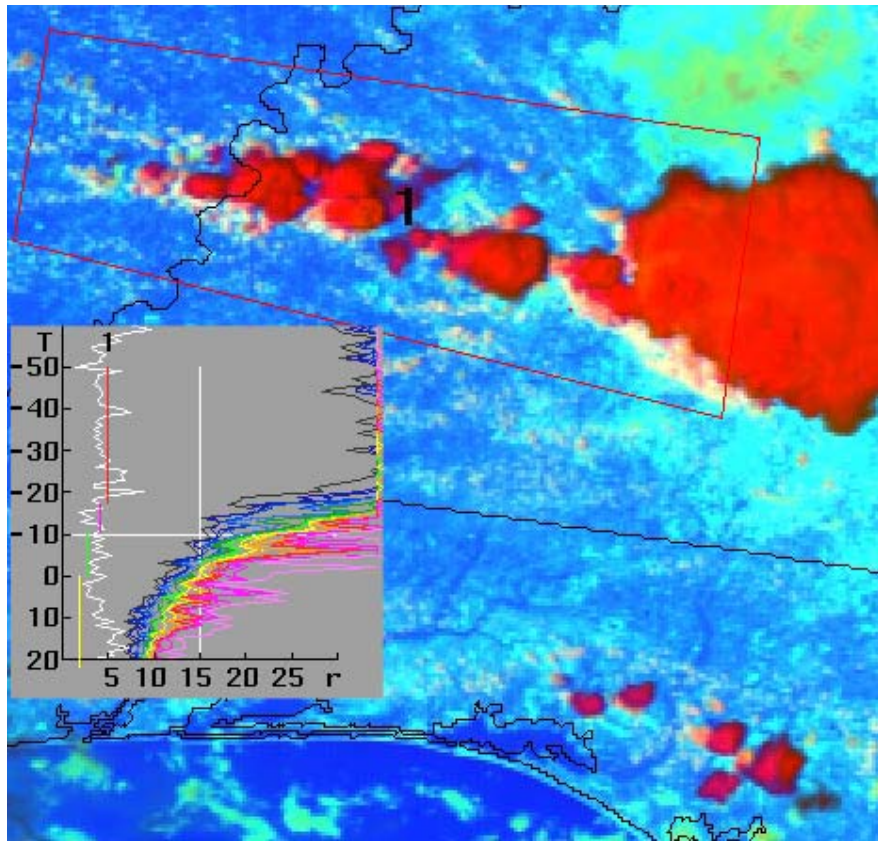


Figure 8a: Same as Fig. 1, but for a non-severe convective storm. The image is based on the NOAA-AVHRR overpass on 28 July 1998, 20:24 UTC, over a domain of 232x222 AVHRR 1-km pixels. The cloud system is just to the north of the Florida Panhandle. Note the rapid increase of r_e towards an early glaciation at -17°C . This is case #9855 (see Appendix), with $T_{\text{base}}=20^\circ\text{C}$, $R_{\text{base}}=8 \mu\text{m}$, $T_{14}=-5^\circ\text{C}$, $TL=-18^\circ\text{C}$, $dTL=38^\circ\text{C}$, $T_g=-20^\circ\text{C}$, $R_g=33.5 \mu\text{m}$ (See parameter definitions in Fig. 9).

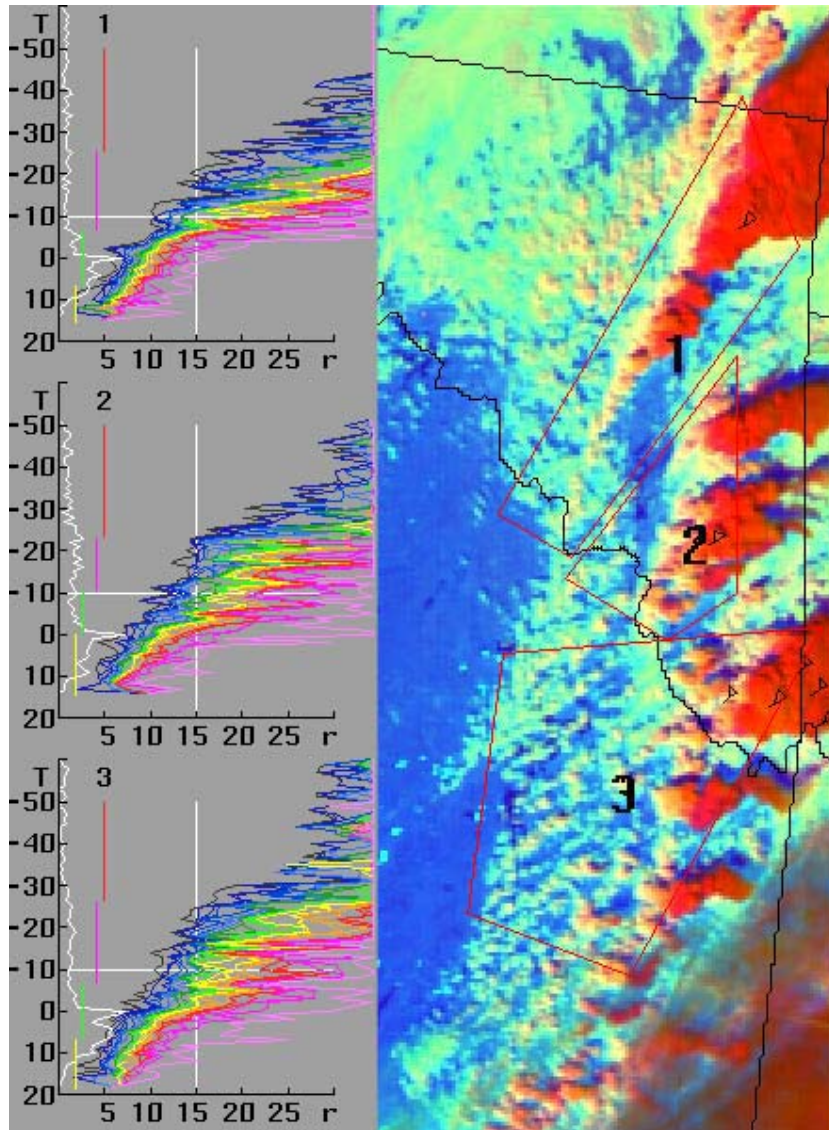


Figure 8b: Same as Fig. 1, but for three hail storms. The image is based on the NOAA-AVHRR overpass on 5 March 1999, 21:32 UTC, at a domain of 220x300 AVHRR 1-km pixels. The cloud system is near the eastern border of Oklahoma. The locations of reported hail (0.75-1.75 inch) are marked by small triangles. Note the deep supercooled layer with glaciation temperature of about -25 for the median r_e (denoted by the bottom of the vertical red line), and less than -30°C for the smallest r_e . This is case #9901 (see Appendix), with $T_{\text{base}}=8^\circ\text{C}$, $R_{\text{base}}=5 \mu\text{m}$, $T_{14}=-12^\circ\text{C}$, $TL=-26^\circ\text{C}$, $dTL=34^\circ\text{C}$, $T_g=-27^\circ\text{C}$, $R_g=32.4 \mu\text{m}$ (See parameter definitions in Fig. 9).

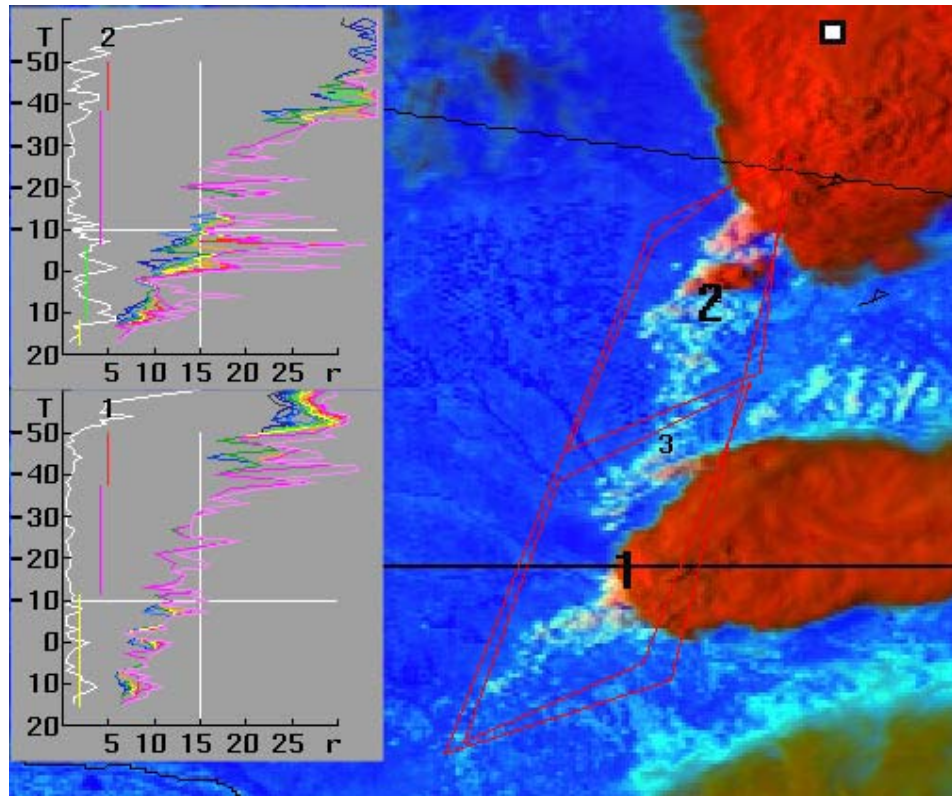


Figure 8c: Same as Fig. 1, but for tornadic storms. The image is based on the NOAA-AVHRR overpass on 29 June 1993, 22:03 UTC, over a domain of 251x210 AVHRR 1-km pixels. The cloud occurred in north central Nebraska. The locations of reported hail and tornadoes within the hour of the image are marked by small triangles and rectangles, respectively. The north storm produced a F2 tornado at 21:49. Note the r_e remaining very small up to the homogeneous freezing temperature of -39°C . The scarcity of points in the interval of -14°C to -38°C disqualifies this case to be included in the analyses.

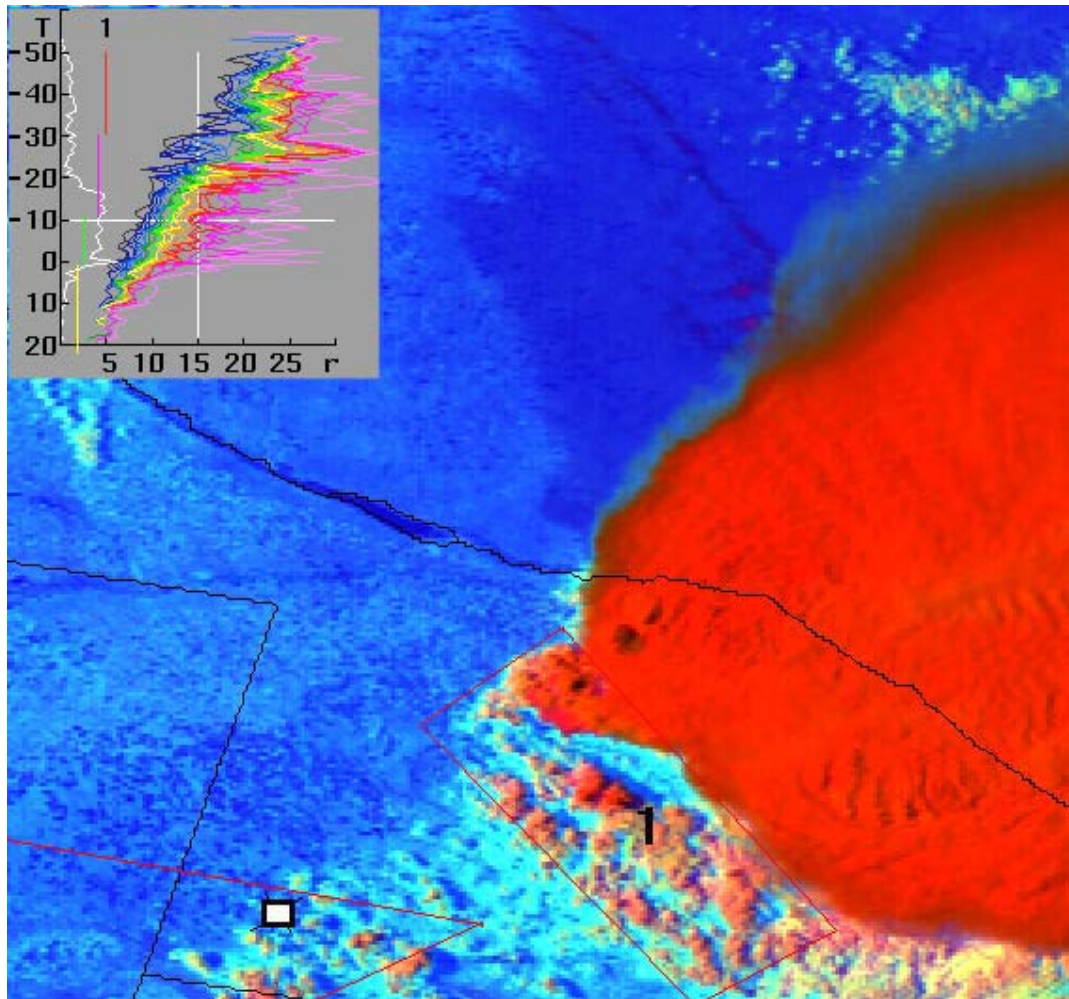


Figure 8d: Same as Fig. 1, but for a tornadic storm with 4.5 inch hail. The image is based on the NOAA-AVHRR overpass on 29 June 2000, 22:21 UTC, over a domain of 282x264 AVHRR 1-km pixels. The cloud occurred in southwestern Nebraska. The locations of a reported F1 tornado at 23:28 is marked by a rectangle. Note that the tornado occurred in a region that had little cloud development 68 minutes before the tornadic event. This demonstrates that there is predictive value in the cloud field before any of the clouds reach severe stature. A hail swath on the ground can be seen as the dark purple line emerging off the north flank of the storm, oriented NW-SE. Two hail gushes are evident on the swath near the edge of the storm. The precipitation swath appears as darker blue due to the cooler wet ground. Note the linear profile of the $T-r_e$ lines, and the glaciation occurs at the small $r_e=25 \mu\text{m}$, in spite of the very warm cloud base temperature near 20°C . This is case #0046 (see Appendix), with $T_{\text{base}}=8^\circ\text{C}$, $R_{\text{base}}=5.5 \mu\text{m}$, $T_{14}=-21^\circ\text{C}$, $T_{\text{L}}=-31^\circ\text{C}$, $dT_{\text{L}}=39^\circ\text{C}$, $T_{\text{g}}=-32^\circ\text{C}$, $R_{\text{g}}=20.6 \mu\text{m}$ (See parameter definitions in Fig. 9).

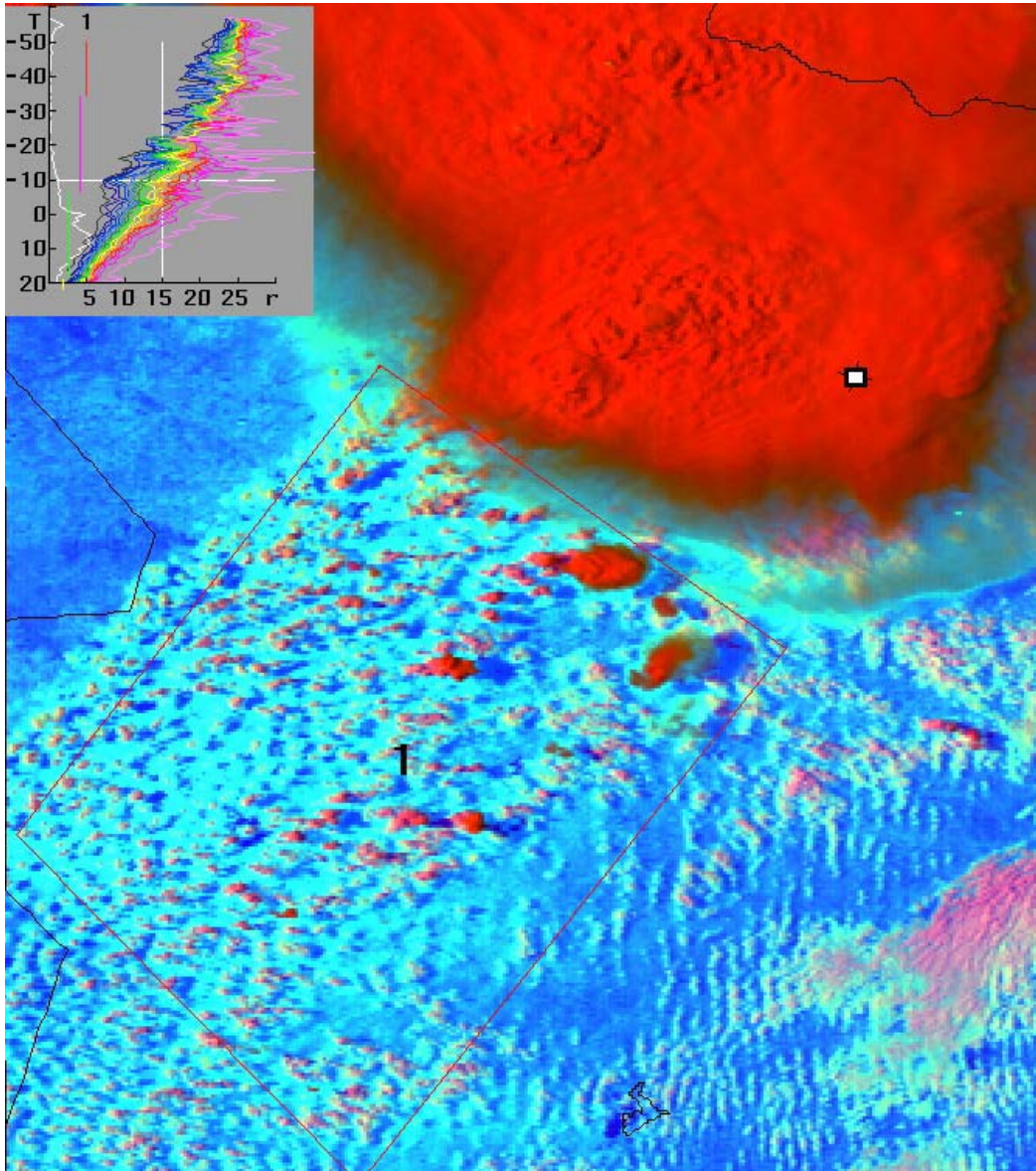


Figure 8e: Same as Fig. 1, but for a tornadic storm with 2.5 inch hail. The image is based on the NOAA-AVHRR overpass on 30 April 2000, 22:14 UTC, over a domain of 333x377 AVHRR 1-km pixels. The cloud occurred just to the SE of the Texas panhandle. The location of a reported F3 tornado at 22:40 is marked by a rectangle. Note the very linear profile of the $T-r_e$ lines, and the glaciation occurs at the small $r_e=25 \mu\text{m}$, in spite of the very warm cloud base temperature of near 20°C , as in Fig. 8d. It is particularly noteworthy that this $T-r_e$ is based on clouds that occurred ahead of the main storm into an area through which the storm propagated. The same is indicated in Fig. 8d, but to a somewhat lesser extent. This is case #0018 (see Appendix), with $T_{\text{base}}=18^\circ\text{C}$, $R_{\text{base}}=4.4 \mu\text{m}$, $T_{14}=-15^\circ\text{C}$, $TL=-37^\circ\text{C}$, $dTL=55^\circ\text{C}$, $T_g=-38^\circ\text{C}$, $R_g=23.9 \mu\text{m}$ (See parameter definitions in Fig. 9).

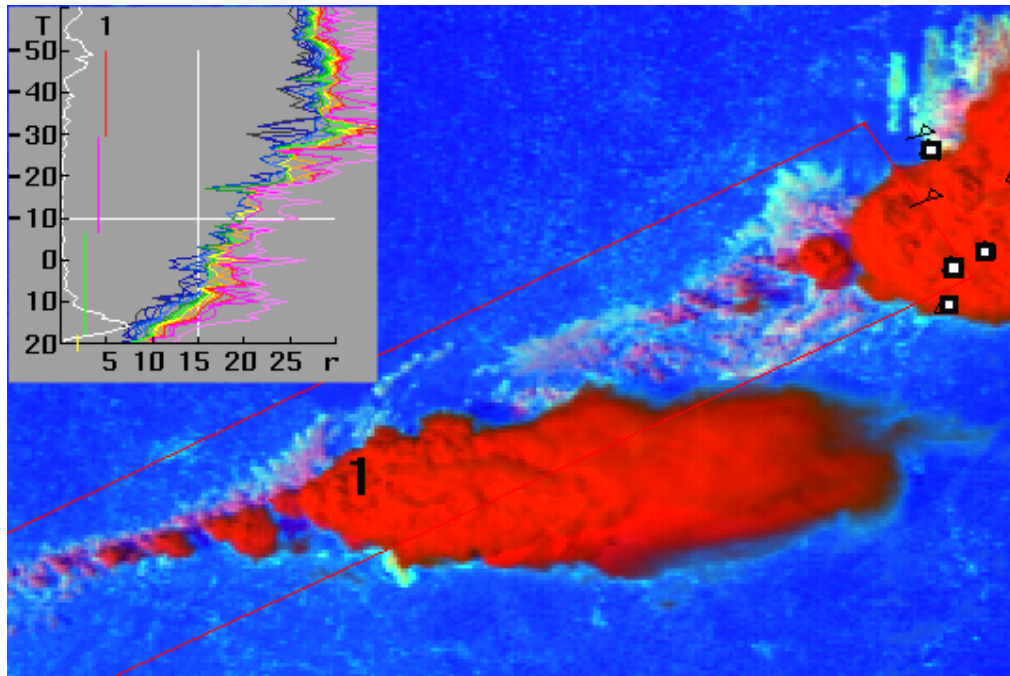


Figure 8f: Same as Fig. 1, but for a tornadic storm with 1.75 inch hail. The image is based on the NOAA-AVHRR overpass on 20 July 1998, 20:12 UTC, over a domain of 262x178 AVHRR 1-km pixels. The cloud occurred in NW Wisconsin. The locations of reported F0 tornadoes are marked by rectangles. Note the large r_e at the lower levels, indicating microphysically maritime microstructure, followed by a very deep mixed phase zone. Very strong updrafts should exist for maintaining such a deep mixed phase zone in a microphysically maritime cloud, as illustrated in line C of Fig. 7A. This is case #9847 (see Appendix), with $T_{base}=16^\circ\text{C}$, $R_{base}=8 \mu\text{m}$, $T_{14}=8^\circ\text{C}$, $TL=-31^\circ\text{C}$, $dTL=47^\circ\text{C}$, $T_g=-32^\circ\text{C}$, $R_g=27.8 \mu\text{m}$ (See parameter definitions in Fig. 9).

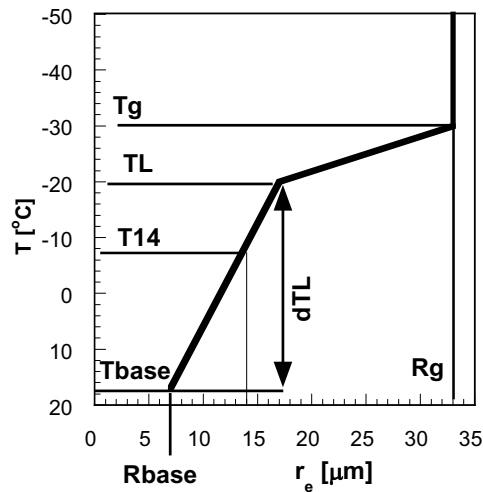


Fig. 9: Illustration of the meaning of the parameters describing the $T-r_e$ relations.

T_{base} : Temperature of cloud base, which is approximated by the warmest point of the $T-r_e$ relation.

R_{base} : The r_e at cloud base.

T_{14} : Temperature where r_e crosses the precipitation threshold of 14 μm .

TL : Temperature where linearity of the $T-r_e$ relation ends upwards.

dTL : Temperature interval of the linear part of the $T-r_e$ relation. $T_{base} - TL$

T_g : Onset temperature of the glaciated zone.

R_g : r_e at T_g

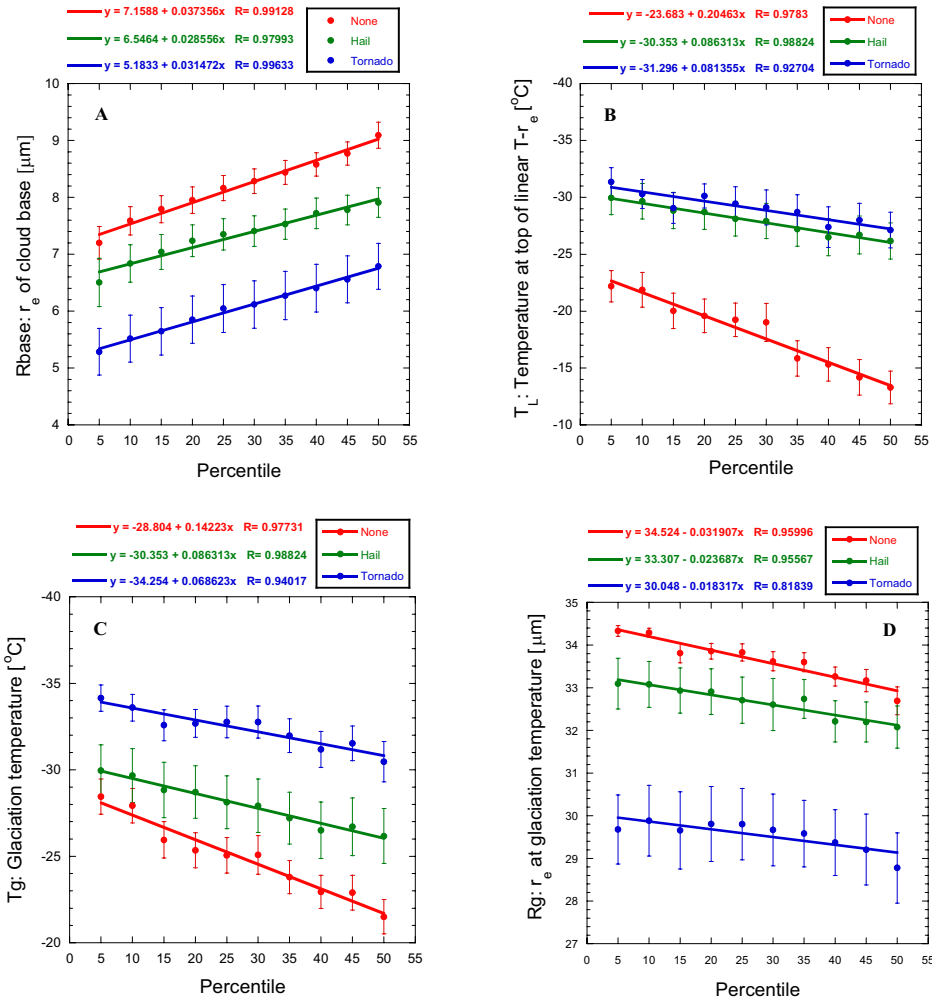


Figure 10: Mean and standard error of the parameterized T-r_e properties for the r_e percentiles of 5, 10, 15,... 50 for a given T, for tornadic, hail only and non-severe storms. Note the obvious increase of r_e at the base with higher percentile, and the decrease of R_{base} for more severe storms (A). Note the decrease in T_L (B), T_g (C) and R_g (D) for the younger and more vigorous cloud elements as represented by the smaller percentiles and for the more severe storms.

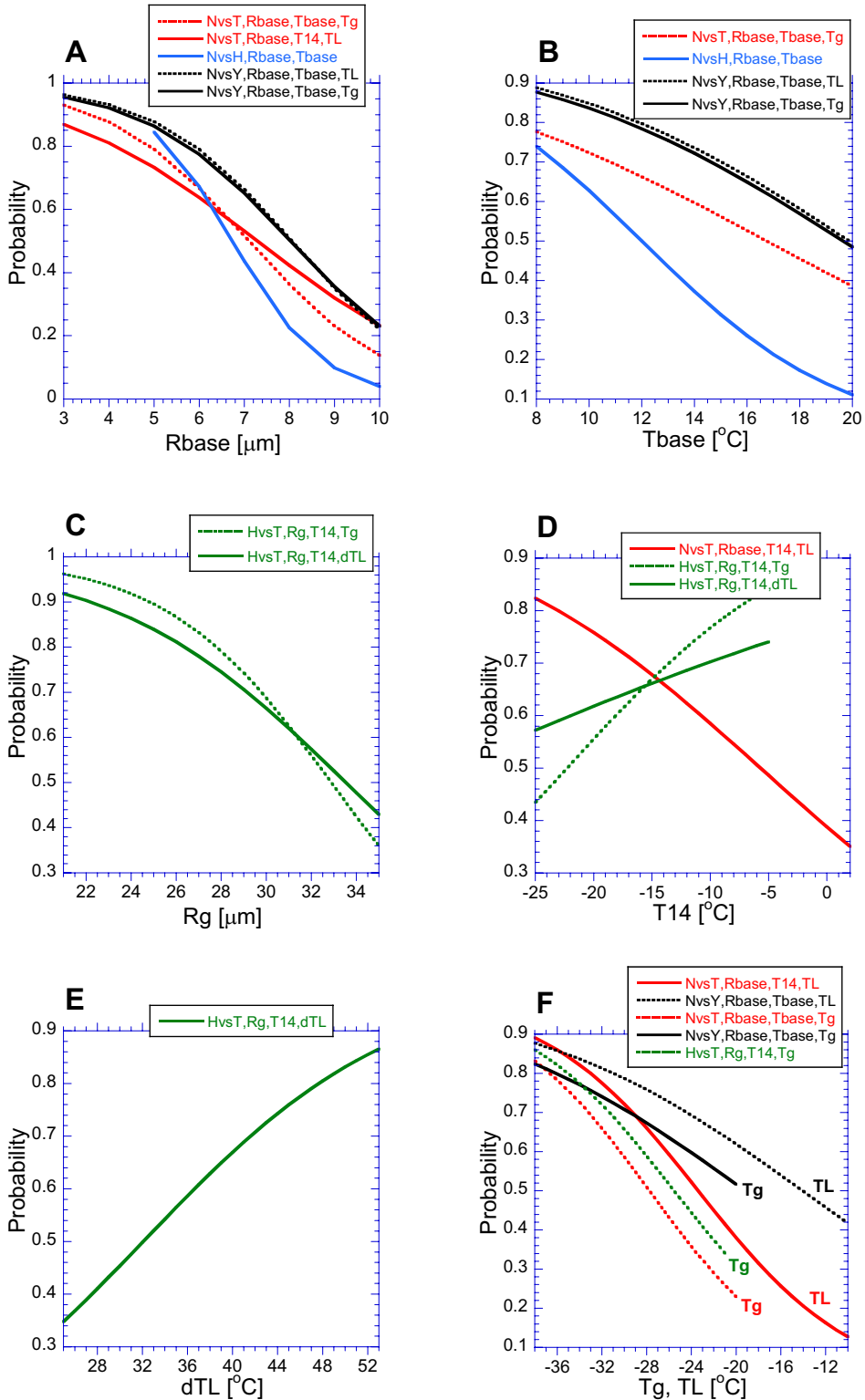


Figure 11: The binary logistic regression probability of discriminating a tornado versus non severe convective storm (NvsT, red), a hail storm versus non severe storm (NvsH, blue) and a tornado versus hail-only storm (HvsT, green), and severe vs. non severe storms (NvsY, black).

The probabilities for the various values of the $T-r_e$ parameters are calculated based on the coefficients in Table 2, when fixing the other parameters at their mean values.

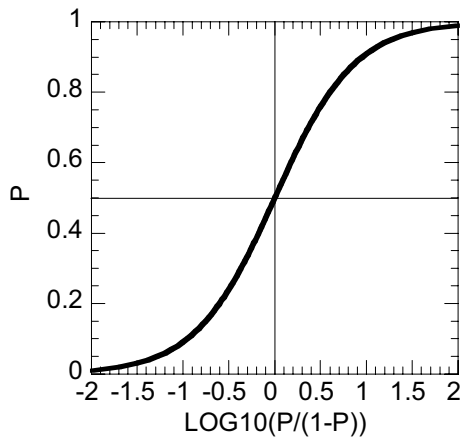


Figure 12: The relations between the probability for an event P and the transformation to $\log_{10}(P/(1-P))$.

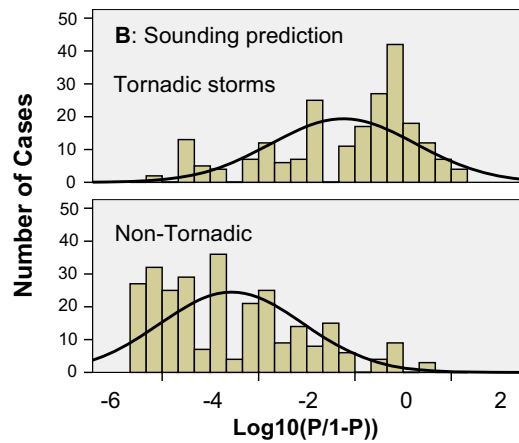
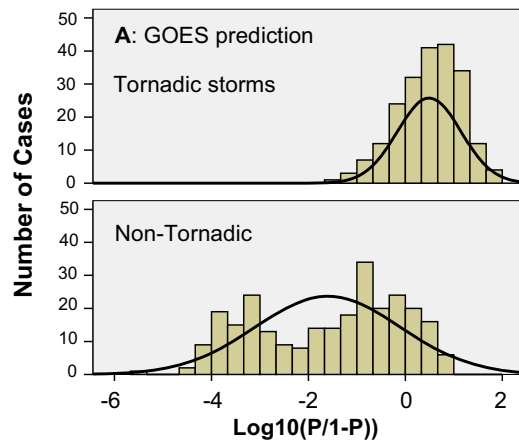


Figure 13: Histograms of the predictions $\log_{10}(P/(1-P))$ for the GOES satellite (A) and the sounding (B) based models. The upper panel is for tornadic scenes, and the lower panel for non tornadic areas.

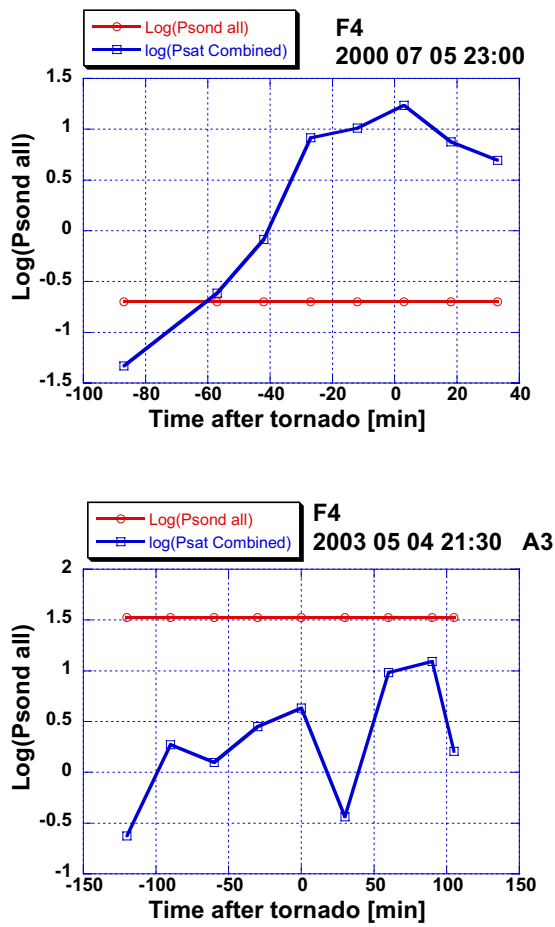


Figure 14: The time dependence of the satellite (blue) and sounding (red) predictors for tornadoes when strong tornadoes occurred.

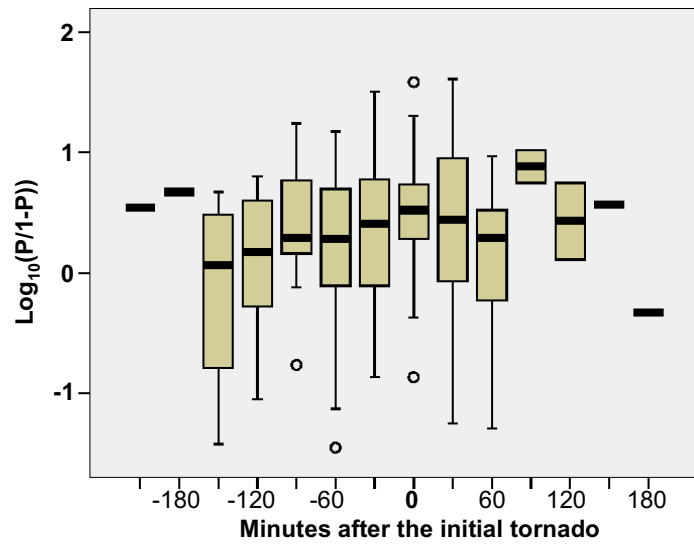


Figure 15: Box plots of the predictions $\log_{10}(P/(1-P))$ as a function of time relative to the time of tornado occurrence for the GOES satellite-combined prediction models (using the appropriate predictor based on cloud base temperature being above or below the 15°C threshold).

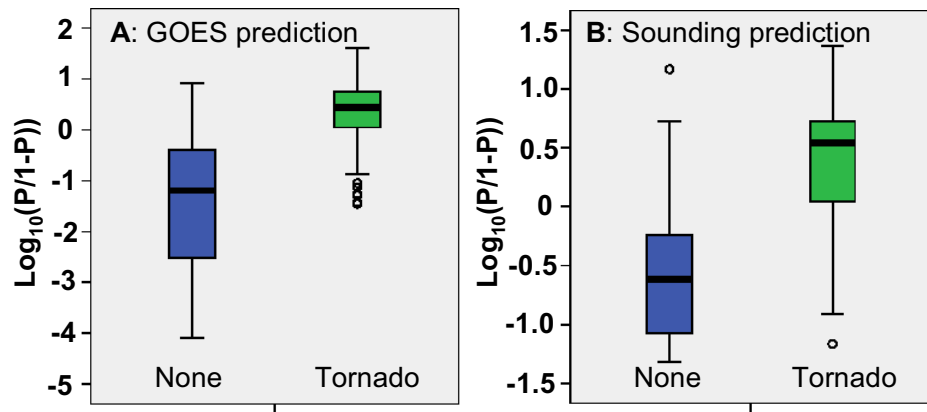


Figure 16: Box plots of the predictions $\log_{10}(P/(1-P))$ for the prediction models, for tornadic and non-tornadic storms. Zero means probability for a tornado $P=0.5$. The left panel is for the satellite prediction. The right panel is the predictor based on the sounding.

Appendix

List of the cases and their parameters that are used in the statistical analysis

Case #	Date mm/dd/yyyy	Event time GMT	Location	Hail size (inch)	Tornado strength (F scale)	Rbase (μm)	Phase (°C)	T _g (°C)	T _L (°C)	T _I (°C)	RG (μm)	DTL (°C)
1	04/23/1998	1940	37	86	N		11.9	-4	-24	-23	-20	32.7
2	04/30/1998	2003	35	87	N		8.8	14	-23	-22	-4	33.4
3	05/03/1998	1931	37	86	N		10	1	-35	-34	-2	30.5
4	05/06/1998	2038	42	100	N		9.6	2	-34	-25	-23	34.8
5	05/26/1998	2018	35	88	N		6.8	16	-28	-14	-9	33.8
6	05/27/1998	2006	37	84	N		8.8	13	-17	-16	-3	34.3
7	06/14/1998	2008	39	92	N		6.8	18	-37	-36	-1	34.3
8	06/22/1998	2021	38	86	N		8.3	13	-19	-16	-7	34.1
9	06/24/1998	1958	37	83	N		7.2	15	-31	-30	-19	34.2
10	06/27/1998	1926	31	83	N		10.9	17	-40	-39	10	33.8
11	07/01/1998	2022	46	94	N		10.9	7	-28	-21	-12	34.9
12	07/01/1998	2022	31	89	N		7.5	19	-31	-21	-6	34.5
13	07/03/1998	2000	33	87	N		8.8	20	-34	-33	2	34.9
14	07/04/1998	1949	38	84	N		7.5	18	-26	-25	3	34.9
15	07/10/1998	2023	36	92	N		6.8	18	-20	-17	-8	34
16	07/10/1998	2023	34	90	N		6.5	20	-23	-22	-3	29.4
17	07/12/1998	2000	31	84	N		5.8	20	-36	-17	-7	34.2
18	07/16/1998	1916	44	75	N		7.5	16	-27	-16	-9	35
19	07/20/1998	2012	31	83	N		6.5	19	-18	-13	-6	33.6
20	07/22/1998	1951	30	83	N		8.3	20	-26	-25	-2	35
21	07/23/1998	1940	33	82	N		7.5	20	-22	-21	4	34.6
22	07/24/1998	1929	36	79	N		6.8	18	-18	-17	-1	33.6
23	07/26/1998	2047	45	89	N		7.5	11	-19	-18	-3	29.5
24	07/28/1998	2024	31	87	N		8	20	-20	-18	-5	34.2
25	07/29/1998	2017	33	88	N		8	19	-26	-19	3	34.1
26	07/29/1998	2017	40	85	N		6.5	20	-20	-9	-9	33.8

27	08/04/1998	2048	32	96	N			7.2	18	-31	-30	-10	34.2	48
28	08/05/1998	2037	34	94	N			7.2	14	-27	4	-9	33.4	10
29	08/08/1998	2003	33	87	N			6.8	20	-30	-15	0	34.9	35
30	08/08/1998	2003	40	84	N			7.2	16	-24	-13	-8	35	29
31	08/09/1998	1953	32	84	N			8.3	20	-27	-26	1	34.1	46
32	08/18/1998	1942	35	81	N			9.2	17	-25	-24	3	33.9	41
33	08/18/1998	1953	33	87	N			9.2	19	-18	-17	3	28.8	36
34	09/24/1998	2128	27	99	N			5.2	20	-19	-12	-1	34.9	32
35	03/24/1999	2123	31	94	N			6.5	16	-20	0	-4	34.4	16
36	04/06/1999	2033	33	87	N			6.5	18	-37	-36	1	33.1	54
37	03/24/1999	2123	33	94	N			7.2	13	-15	0	-3	33.9	13
38	06/04/2000	2206	37	96	N			6.8	17	-23	-18	-5	33.4	35
39	03/05/1998	2030	31133	88.42	H	1		6.1	14	-31	-30	-8	34.2	44
40	04/03/1998	2043	34.63	86.28	H	1.75		7.5	11	-35	-22	-9	35	33
41	04/03/1998	2009	36.53	87.35	H	1.75		4.6	11	-31	-26	-17	34	37
42	04/22/1998	2049	33.98	83.72	H	0.75		7.5	0	-24	-16	-17	34	16
43	04/22/1998	2030	34.07	78.53	H	0.75		6.5	4	-26	-22	-20	32.5	26
44	04/22/1998	2007	33.65	83.72	H	1		8.8	1	-40	-16	-17	34.7	17
45	05/04/1998	2019	36.78	76.97	H	0.75		8.3	9	-16	-14	-7	34.1	23
46	05/07/1998	2100	35.07	86.43	H	0.75		7.2	10	-26	-18	-11	34.1	28
47	05/24/1998	2030	38.78	100.38	H	2.5		7.5	13	-36	-35	-11	33.6	48
48	06/11/1998	2100	44.93	96.73	H	1		11.4	12	-25	-24	-7	34.2	36
49	06/15/1998	2054	38.75	77.48	H	1.75		9.2	10	-22	-12	-12	34.2	22
50	06/16/1998	2012	39.28	80.35	H	2.75		6.8	9	-32	-26	-13	34	35
51	07/17/1998	2019	30.72	95.53	H	1.75		5.8	18	-25	-18	-15	33.7	36
52	08/06/1998	2107	30.07	82.23	H	1.75		6.5	18	-20	-16	-4	34.4	34
53	08/07/1998	2004	32.73	82.72	H	0.75		6.5	20	-16	-12	-7	34.3	32
54	08/11/1998	2034	34.93	104.82	H	0.75		6.8	8	-38	-37	-15	33	45
55	09/09/1998	2034	37.17	101.17	H	0.88		8.3	10	-38	-37	-7	33.9	47
56	03/05/1999	2149	36.7	94.97	H	1		4.9	8	-27	-26	-12	33.3	34
57	03/08/1999	2025	30.58	96.08	H	1.75		8	18	-13	-12	3	24.9	30
58	04/07/1999	2107	32.62	83.6	H	2		5.8	13	-28	-27	-6	34.4	40
59	06/08/1999	2245	33.38	104.52	H	1.75		5.5	20	-34	-29	-30	27.7	49
60	03/05/1999	2234	35.48	94.23	H	4.5		4.9	13	-32	-26	-14	34	39

61	05/07/1995	2040	31.03	100.82	H	2.5		6.8	16	-39	-38	-23	27.5	54
62	06/13/1992	2207	33.82	102.25	H	2		5.5	13	-38	-33	-24	30.7	46
63	05/02/1998	2042	39.98	88.25	T	0.75	0	7.5	3	-39	-38	-10	34.4	41
64	05/15/1998	2115	41.08	92.52	T	1.75	0	7.5	17	-29	-15	-12	34.2	32
65	07/20/1998	2028	47.6	96.18	T	1.75	0	8	16	-32	-31	8	31.2	47
66	03/12/1999	2040	31.04	99.03	T	2	2	1.8	19	-33	-32	-24	32.7	51
67	04/02/1999	2145	36.24	97.05	T	1.75	0	3.9	20	-38	-37	-6	33.9	57
68	06/18/1999	2219	37.27	100.48	T	2.75	1	7.5	10	-32	-30	-21	34.2	40
69	06/04/1995	2000	34.38	102.35	T	4.5	1	3.9	16	-31	-30	-19	20.2	46
70	06/08/1993	2131	41.1	83.78	T	3.5	1	5.8	17	-32	-30	-11	34.6	47
71	06/08/1993	2225	43.65	89.32	T	1.75	2	5.2	15	-33	-32	-3	34.6	47
72	06/06/1992	2158	32.13	102.77	T	1.75	0	10.9	14	-37	-36	-8	27.8	50
73	06/18/1992	2100	38.28	85.05	T	1.75	1	8	18	-29	-19	-17	33.8	37
74	06/21/1992	2000	33.95	82.17	T	2	1	6.1	13	-35	-34	-13	33.1	47
75	04/11/2000	2335	31.2	101.11	T	2.75	0	3.2	15	-40	-39	-15	29.4	54
76	04/16/2000	2039	38.43	90.78	T	1	0	6.1	11	-26	-25	-8	34.5	36
77	04/23/2000	2158	33.05	94.38	T	1.75	3	6.5	15	-38	-37	-12	28.9	52
78	04/30/2000	2240	34.01	100.8	T	1.25	3	4.4	18	-38	-37	-15	25.1	55
79	05/12/2000	2136	44.18	84.2	T	0.88	0	8.8	13	-34	-33	-9	33.6	46
80	05/17/2000	2215	40.95	100.36	T	2.5	3	4.9	9	-34	-28	-23	29.8	37
81	05/25/2000	2327	33.63	101.98	T	2.75	0	4.1	11	-32	-31	-29	23.5	42
82	05/26/2000	2258	33.16	99.75	T	1.75	0	5.8	19	-38	-37	-9	23.9	56
83	06/29/2000	2329	40.21	101.75	T	4.5	1	5.5	8	-32	-31	-21	23.1	39
84	07/11/2000	2255	43.96	97.16	T	4	2	8	16	-25	-24	4	34.2	40
85	07/21/2000	2350	40.38	104.25	T	2	1	2.3	1	-38	-32	-34	24.5	33
86	07/24/2000	2305	43.23	100.06	T	2.75	0	1.7	20	-38	-37	-13	29.3	57
87	03/08/2001	2315	30	98	T	1.75	0	1.8	13	-38	-23	-16	35	36
88	04/12/2001	2400	38	99	T	1.75	0	6.1	10	-21	-20	-10	24.1	30
89	05/01/2001	2402	44	94	T	1	2	3	10	-39	-38	-37	17.4	48
90	05/09/2001	2334	42	97	T	1	0	4.1	13	-39	-38	-23	25.3	51
91	07/09/1998	2130	40.62	102.47	T		0	10	15	-21	-13	4	35	28
92	08/05/1995	2000	41.2	102.47	T		0	8	4	-33	-32	-13	34.2	36
93	06/22/1993	2240	41.2	102.47	T		0	8.8	3	-29	-28	-29	22.7	31
94	07/20/1993	2133	34.78	76.82	T		0	6.8	18	-31	-30	-5	35	48

95	06/22/2000	2235	33.96	98.68	T		0	7.2	20	-28	-27	7	33.8	47
96	08/30/2000	2230	30.96	89.8	T		0	2.3	20	-35	-34	-17	28.2	54